

1 **The impact of lateral boundary forcing in the CORDEX-Africa
2 ensemble over southern Africa**

4 Maria Chara Karypidou¹, Stefan Pieter Sobolowski², Lorenzo Sangelantoni^{3,4}, Grigory Nikulin⁵, Eleni Katragkou¹

5 ¹Department of Meteorology and Climatology, School of Geology, Faculty of Sciences, Aristotle University of
6 Thessaloniki, Thessaloniki, Greece

7 ²NORCE Norwegian Research Centre, Bjerknes Centre for Climate Research, Bergen, Norway

8 ³CETEMPS—Department of Physical and Chemical Sciences, University of L’Aquila, L’Aquila, Italy

9 ⁴Department of Physical and Chemical Sciences, University of L’Aquila, L’Aquila, Italy

10 ⁵Rossby Centre, Swedish Meteorological and Hydrological Institute, Norrköping, Sweden

11 Corresponding author: Maria Chara Karypidou, karypidou@geo.auth.gr

12 **Abstract**

15 The region of southern Africa (SAF) is among the most exposed climate change hotspots and is projected to experience
16 severe impacts on multiple economical and societal sectors. For this reason, producing reliable projections of the
17 expected impacts of climate change is key for local communities. In this work we use a set of 19 regional climate
18 models (RCMs) performed in the context of the Coordinated Regional Climate Downscaling Experiment (CORDEX)
19 – Africa and a set of 10 global climate models (GCMs) participating in the Coupled Model Intercomparison Project
20 Phase 5 (CMIP5), that were used as the driving GCMs in the RCM simulations. We are concerned about the degree
21 to which RCM simulations are influenced by their driving GCMs, with regards to monthly precipitation climatologies,
22 precipitation biases and precipitation change signal, according to the Representative Concentration Pathway (RCP)
23 8.5 for the end of the 21st century. We investigate the degree to which RCMs and GCMs are able to reproduce specific
24 climatic features over SAF and over three sub-regions, namely the greater Angola region, the greater Mozambique
25 region and the greater South Africa region. We identify that during the beginning of the rainy season, when regional
26 processes are largely dependent on the coupling between the surface and the atmosphere, the impact of the driving
27 GCMs on the RCMs is smaller, compared to the core of the rainy season, when precipitation is mainly controlled by
28 the large-scale circulation. In addition, we show that RCMs are able to counteract the bias received by their driving
29 GCMs, hence, we claim that the cascade of uncertainty over SAF is not additive, but indeed the RCMs do provide
30 improved precipitation climatologies. The fact that certain bias patterns over the historical period (1985-2005)
31 identified in GCMs are resolved in RCMs, provides evidence that RCMs are reliable tools for climate change impact
32 studies over SAF.

37 **1 Introduction**
38

39 The region of southern Africa (SAF) is among the most exposed climate change hotspots (Diffenbaugh and Giorgi,
40 2012) and is projected to experience severe impacts on multiple economical and societal sectors (Conway et al., 2015;
41 Masipa, 2017; Shew et al., 2020). Poverty, food insecurity and high levels of malnutrition (Misselhorn and Hendriks,
42 2017) render SAF a region particularly vulnerable to the impacts of climate change (Casale et al., 2010; Luan et al.,
43 2013; Wolski et al., 2020). In addition, the population's reliance on rain-fed agriculture makes strategic planning
44 necessary as it aims to mitigate the impact of climate change on local communities.

45 Global climate models (GCM) participating in the Coupled Model Intercomparison Project Phase 5 (CMIP5) (Taylor
46 et al., 2012) project a significant decline in annual precipitation over SAF (IPCC and Stocker, 2013), with the most
47 pronounced changes projected under representative concentration pathway 8.5 (RCP8.5) (Sillmann et al., 2013). This
48 reduction is also identified in the regional climate model (RCM) simulations performed in the context of the
49 Coordinated Regional Climate Downscaling Experiment (CORDEX) – Africa domain (Nikulin et al., 2012; Giorgi
50 and Gutowski, 2015). More specifically according to CORDEX-Africa simulations, annual precipitation is expected
51 to decline by up to 50% by the end of the 21st century (Pinto et al., 2018), while duration of dry spells is projected to
52 increase (Dosio et al., 2019). Despite this, extreme rain events are expected to increase in frequency and intensity
53 (Pinto et al., 2016; Abiodun et al., 2019). Nevertheless, for a global warming level of 2 °C, certain parts of SAF
54 (northern Angola, Zambia, northern Mozambique and eastern South Africa) are projected to experience precipitation
55 increase during specific times of the year (Maíre et al., 2018).

56 The question of whether or not RCMs produce demonstrable added value relative to their driving GCMs, has often
57 fueled debate between the RCM and GCM modelling communities (Lloyd et al., 2020). The outcome of the debate is
58 not binary. The literature provides ample evidence that there is indeed evidence of added value in RCMs, but it is
59 dependent on the region examined, on the season, and the climate mechanisms that are at play (Luca et al., 2016, Feser
60 et al., 2011). RCM ensembles such as those in CORDEX-Africa endeavor to provide added value, by dynamically
61 downscaling historical and scenario simulations originating from coarse resolution GCMs (Dosio et al., 2019). The
62 added value in RCM simulations arises as a result of their higher horizontal resolution (<50 km), which makes it
63 possible for atmospheric waves and synoptic scale disturbances to be represented in a more realistic manner. An
64 additional aspect that further contributes towards this end, is the more accurate representation of land surface
65 characteristics (topography, land use etc.) in RCMs (Di Luca et al., 2013). Moreover, the physics of an RCM can be
66 targeted for processes specific to the region it is being run for, giving it a local advantage over GCMs that may have
67 had their physics developed for global applications. Nevertheless, RCMs also are accompanied by a set of model
68 deficiencies that affect the final output of the downscaled data (Boberg and Christensen, 2012). In Sørland et al. (2018)
69 it is reported that although RCM biases are affected by the driving GCMs, they are nonetheless not additive, a result
70 that counters the common “cascade of uncertainty” criticism. Still, uncertainty arising from both the driving GCM
71 (Moalafhi et al., 2017) and the downscaling RCM affect the final product (Nikulin et al., 2012), and it is important to
72 diagnose the sources and causes of these errors (Déqué et al., 2012).

73 Attributing this uncertainty into its respective components is key for a better assessment of the reliability of RCM
74 simulations (Christensen and Kjellström, 2020). GCMs provide the lateral boundary conditions to the RCMs and each
75 RCM receives, absorbs, and modulates the received atmospheric forcing in different ways, depending on the numerical
76 formulations and parameterization schemes employed. Discerning between the signal received by the GCM and the
77 signal produced by the RCM is critical for assessing the robustness with which different modelling systems are able
78 to accurately reproduce observed climatologies and generate reliable estimates of the expected climate change. In
79 addition, the manner in which an RCM responds to the atmospheric forcing provided by a GCM can be region specific
80 (Rana et al., 2020; Wu and Gao, 2020) (e.g., regions located in close proximity to the boundaries of the RCM domain
81 can be more severely affected by the driving GCMs, than regions at the center of the RCM domain or there can be
82 region specific response around complex topography versus lowlands). Also, the degree to which an RCM is
83 influenced by the driving GCM can be process specific. For instance, when there is a strong large-scale circulation
84 signal that is introduced to an RCM domain (e.g. advective mid-latitude storms), it is quite likely that the RCM will
85 be able to reproduce the information that is received at its lateral boundaries, however, the GCM's impact on the RCM
86 simulation may also vary depending on how far a region lies from the RCM domain boundaries (Kim et al., 2020). If,
87 however, the large-scale forcing is weak, then the atmospheric conditions simulated within the RCM domain are more
88 dependent on the dynamic and thermodynamic processes employed by the RCM (e.g. convective thunderstorms).
89 In this work we aim to assess whether it is the RCMs or their driving GCMs that dominate monthly precipitation
90 climatology, monthly precipitation bias and climate change signal over SAF. We take into account the region-specific
91 characteristics of this question by analyzing SAF and three subregions, namely southeastern Angola, Mozambique
92 and South Africa. We also consider the different atmospheric processes that are in play over each region by analyzing
93 monthly climatologies. Precipitation over SAF results from various atmospheric processes that are highly variable
94 during the rainy season (Oct-Mar), so by performing the analysis on a monthly basis, we are able to indirectly study
95 how certain processes are reproduced by GCM and RCM simulations. In order to differentiate between the signal
96 emanating from the RCMs and their driving GCMs, we use the analysis of variance (ANOVA) in both the GCM and
97 the RCM ensembles (Déqué et al., 2007, 2012). Since the information provided by RCMs will eventually be used by
98 both climate and non-climate scientists, especially in light of climate change impact studies, we aim to provide some
99 information with regards to how much each RCM output is affected by its driving GCM and what climate change
100 signals are identified consistently in both RCMs and GCMs.

101

102 **2 Material and methods**

103 **2.1 Data**

104 The data analyzed in the current work consist of RCM simulations performed in the context of CORDEX-Africa, a
105 set of simulations performed in the context of CMIP5, and the CHIRPS satellite rainfall product (Funk et al., 2015).
106 More specifically, the CORDEX-Africa simulations selected are those that were driven by more than two GCMs (at
107 least three simulations available using the same RCM driven by at least three different GCMs) and for which there are
108 runs available for both the historical and the future period under RCP8.5. All RCMs employed a relaxation zone which

109 was either 10 grid-points wide (CCLM4-8-17.v1) or eight points wide (RCA4.v1 and REMO2009.v1). Relaxation in
110 all RCM simulations was performed using Davie's method (Davies, 1976, 1983). The CMIP5 GCMs selected are the
111 ones that were used to drive the CORDEX-Africa simulations. All RCM and GCM simulations were retrieved from
112 the Earth System Grid Federation (<https://esgf-data.dkrz.de/projects/esgf-dkrz/>). The CHIRPS rainfall product is used
113 for calculating precipitation biases in both the CORDEX-Africa and CMIP5 ensembles and was retrieved from:
114 <https://www.chc.ucsb.edu/data/chirps>. CHIRPS is available at 5 km spatial resolution and for the calculation of biases
115 it was remapped to the coarser resolution grid using conservative remapping. A fact that is commonly obscured is that
116 observational datasets are often considered as "ground truth" however, they also are subject to multiple sources of
117 uncertainty, caused by the underlying station datasets used, the statistical algorithms employed in spatially interpolated
118 methods or the algorithms employed in satellite rainfall products (Le Coz and van de Giesen, 2020). More specifically,
119 over southern Africa, it was found that gauge-based products employing spatial interpolation methods displayed high
120 uncertainty over regions where the underlying station network was scarce, mainly over the Angola region and the
121 northern parts of SAF (Karypidou et al., 2022). In addition, it was found that this attribute was inherited by all rainfall
122 satellite products that were using direct merging techniques with gauge-based datasets. Here, we display monthly
123 precipitation during the historical period (1985-2005) across four observational datasets, given in **Table 1**. More
124 specifically, we use the CRUv4.06 dataset (Harris et al., 2020), which is a purely gauge-based product (employing
125 station data and a spatial interpolation algorithm to provide a spatially continuous gridded product), ERA5 (Hersbach
126 et al., 2020), which is a reanalysis product, CHIRPS (Funk et al., 2015), which is a satellite rainfall product, and
127 finally, MSWEP (Beck et al., 2017) which is a product merging station data, satellite data and dynamic model outputs.
128 All datasets have been analyzed using monthly mean values. The results are displayed in **Fig. 1**. As shown, there is a
129 substantial agreement among them both with regards to the spatial and temporal pattern of monthly precipitation over
130 southern Africa.

131

132 Table 1 Gauge-based, satellite, reanalysis and merged precipitation products analyzed over the study region using
133 monthly mean precipitation for the period 1985-2005.

Dataset	Resolution	Frequency	Type	Period
CRU TS4.06	0.5°	Monthly total	Gauge-Based	1901-2021
MSWEP	0.1°	3-hourly	Merged product	1979-present
CHIRPS.v2	0.05°	Daily totals	Satellite	1981-present
ERA5	~0.25 °	Hourly	Reanalysis	1979-present

134

135 Our analysis is split into two sections: the qualitative and the quantitative part. In the qualitative part, we aim to
136 identify if RCMs exhibit systematic behavior relative to their driving GCMs. For the quantitative part, we aim to
137 quantify the degree to which monthly precipitation climatologies, biases and climate change signal are affected by
138 the downscaled RCMs or by the GCMs driving the RCM simulations. For this purpose, we employ an ensemble of 19
139 RCM simulations driven by 10 GCMs and the driving GCMs that were used to provide the lateral boundary conditions
140 to the RCMs. From the historical simulations we use the period 1985-2005 and from the projection simulations we
141 use the period 2065-2095 under RCP8.5. All CORDEX-Africa simulations are available at ~50 km horizontal
142 resolution and are shown in **Table 1**, while the horizontal resolution for the driving GCMs is provided in **Table 3**.

143

144 **Table 2** Input RCM and GCM simulations used. The CORDEX-Africa simulations are given in the columns. The
 145 CMIP5 GCMs used as driving fields are given in the rows.

	CCLM4-8-17.v1	RCA4.v1	REMO2009.v1
CanESM2		✓	
CNRM-CM5	✓	✓	
EC-EARTH	✓	✓	✓
HadGEM2-ES	✓	✓	✓
MIROC5		✓	✓
MPI-ESM-LR	✓	✓	✓
IPSL-CM5A-LR			✓
IPSL-CM5A-MR		✓	
CSIRO-Mk3-6-0		✓	
GFDL-ESM2M		✓	
NorESM1-M		✓	

146

147 **Table 3** Horizontal resolution of the CMIP5 GCMs used as driving fields in the CORDEX-Africa simulations.

GCMs	Latitude Res.	Longitude Res.	References
CanESM2	2.7906 °	2.8125 °	(CCCma, 2017)
CNRM-CM5	1.40008 °	1.40625 °	(Volodire et al., 2013)
CSIRO-Mk3-6-0	1.8653 °	1.875 °	(Jeffrey et al., 2013)
EC-EARTH	1.1215 °	1.125 °	(Hazeleger et al., 2010)
GFDL-ESM-2M	2.0225 °	2.5 °	(Dunne et al., 2012)
HadGEM2-ES	1.25 °	1.875 °	(Collins et al., 2011)
IPSL-CM5A-MR	1.2676 °	2.5 °	(Dufresne et al., 2013)
IPSL-CM5A-LR	1.894737 °	3.75 °	
MIROC5	1.4008 °	1.40625 °	(Watanabe et al., 2010)
MPI-ESM-LR	1.8653 °	1.875 °	(Giorgetta et al., 2013)
NorESM1-M	1.894737 °	2.5 °	(Bentsen et al., 2013)

148

149 **2.2 Methods**

150 The study region and subregions considered are depicted in **Fig. 2**. The subregions are selected based on particular
 151 phenomena and processes that are of importance for the seasonal cycle of precipitation. More specifically, Region A
 152 (hereafter: SAF-All) encompasses the entire SAF region and is defined as the area extending from 10 °E to 42 °E and
 153 from 10 °S to 35 °S. Region B (hereafter: Angola region) was selected to capture the main region of interest with
 154 regards to the Angola Low (AL) pressure system (Howard and Washington, 2018) and covers the area extending from
 155 14 °E to 25 °E and from 11 °S to 19 °S. Region C (hereafter: East Coast) covers the eastern coastline, Mozambique and
 156 surrounding countries and extends from 31 °E to 41 °E and from 10 °S to 28 °S. Lastly, we define the SAfr region,
 157 which covers much of South Africa and extends from 15 °E to 33 °E and from 26 °S to 35 °S.

158 One of the primary synoptic scale features controlling precipitation over SAF is the Angola Low (AL) pressure system
 159 (Reason and Jagadheesha, 2005; Lyon and Mason, 2007; Crétat et al., 2019; Munday and Washington, 2017; Howard
 160 and Washington, 2018), which has a distinct seasonal cycle throughout the rainy season (Oct-Mar). This motivates its

161 selection as a subregion for our study. The AL exhibits heat low characteristics during Oct-Nov and tropical low
162 characteristics during Dec-Feb (Howard and Washington, 2018). This suggests that during Oct-Nov, since
163 precipitation is thermally induced and thus tightly dependent on land-atmosphere interactions, it will be the RCMs
164 that are dominant in controlling precipitation processes. As the rainy season progresses, the AL changes to a tropical
165 low pressure system and its formation is controlled by the large-scale circulation that is characterized by easterly
166 winds from the Indian Ocean that enter SAF via the Mozambique channel. Since precipitation during Dec-Feb is
167 caused by the tropical low phase of the Angola low pressure system, which is the monthly aggregate of frequent
168 transient low pressure systems crossing southern African (Munday and Washington, 2017; Howard and Washington,
169 2018; Howard et al., 2019), we hypothesize that the impact of the driving GCM fields during Dec-Feb is enhanced.
170 In addition, the wider area of Mozambique is a region where the majority of tropical cyclones/depressions make
171 landfall over continental SAF. The occurrence of transient low-pressure systems is enhanced during the core of the
172 rainy season (Dec-Feb) and thus we are interested in identifying whether the impact of the driving GCMs is dominant
173 during Dec-Feb. Also, since according to (Muthige et al., 2018), the number of landfalling tropical cyclones under
174 RCP8.5 is expected to decline in the future, we are interested in examining whether the impact of the driving GCMs
175 to the RCM simulations will be altered under future conditions. Hence, the East Coast region is used as a region
176 indicative of the landfalling tropical cyclones/depressions. Lastly, we examine the area encompassing South Africa
177 (hereafter: SAfr) due to its strong land-ocean gradients, complex topography and strong seasonal variations in rainfall
178 zones.

179

180 **2.2.1 Monthly precipitation climatology and bias**

181 In order to assess whether or not the RCMs improve the monthly precipitation climatologies relative to their driving
182 GCMs, we employ a method initially described in Kerkhoff et al. (2015) and later employed by Sørland et al. (2018),
183 which displays in a scatterplot form the RCM increment as a function of the GCM bias. More specifically, the RCM
184 increment is described as the difference of each RCM simulation from its driving GCM (RCM-GCM). The RCM
185 increment is plotted against the GCM bias (GCM-OBS). This plot displays whether or not the RCM increment
186 counteracts the GCM bias. If the RCM increment reduces the GCM bias, then points are expected to lie along the $y=x$
187 line (negative correlation). On the contrary, if the RCM increment increases the GCM bias, then points are expected
188 to lie along the $y=x$ line (positive correlation). If the RCM increment and the GCM bias are independent, then points
189 are expected to be scattered randomly.

190

191 **2.2.2 Climate change signal**

192 The climate change signal (CCS) is identified as the monthly mean difference between the future period (2065-2095)
193 minus the historical period (1985-2005). As an exploratory method of inspecting the differences between each RCM
194 simulation from its respective driving (GCM) for monthly precipitation during both the historical and the future period,
195 we subtract the downscaled precipitation field (RCM_{DRI}) from its driving (DRI), as in **Eq. 1**:

$$DIFF = RCM_{DRI} - DRI \quad \text{Eq. 1}$$

196 If $DIFF > 0$ (monthly precipitation), then we assume that the RCM enhances precipitation, relative to its driving GCM,
 197 while if $DIFF < 0$ then we assume that the RCM reduces precipitation, relative to its driving GCM. This method is
 198 employed in the qualitative part of the analysis.

199

200 2.2.3 Analysis of variance

201 Additionally, we employ an ANOVA decomposition (Déqué et al., 2007, 2012), in order to understand whether it is
 202 the RCMs or their respective driving GCMs that are responsible for controlling precipitation over the historical (1985-
 203 2005) period and the future period (2065-2095). For this purpose, we use two quantities, namely the “inter-RCM”
 204 variance and the “inter-GCM” variance, as in (Déqué et al., 2012). More specifically, the “inter-RCM variance” is the
 205 variance between all the RCM simulations that are driven by the same GCM. Subsequently, all variances obtained for
 206 all driving GCMs are averaged.

$$RCM_{var} = \frac{1}{N_{RCM}} \sum_{RCM_j} (P_j - \bar{P}_j)^2 \quad \text{Eq. 2}$$

207 The quantity P_j is the monthly precipitation obtained from all RCMs (j) that were driven by the same GCM. The
 208 quantity \bar{P}_j is the mean monthly precipitation obtained by all RCMs (j) that share a common driving GCM. As a final
 209 step, the average of all variances is calculated.

$$Inter_RCM_{var} = \frac{\sum GCM_j}{N} \quad \text{Eq. 3}$$

210 Similarly, the “inter-GCM” variance describes the variance between all the GCMs that were used to drive a single
 211 RCM and then averaged over all the variances obtained for all driven RCMs. N refers to all available simulations
 212 contributing to either the inter-RCM or inter-GCM variance.

$$GCM_{var} = \frac{1}{N_{GCM}} \sum_{GCM_i} (P_i - \bar{P}_i)^2 \quad \text{Eq. 4}$$

213 Likewise, the average of all variances is calculated.

$$Inter_GCM_{var} = \frac{\sum RCM_i}{N} \quad \text{Eq. 5}$$

214 Both “inter-RCM” and “inter-GCM” variances are normalized by the total variance obtained for all months, as in
 215 (Vautard et al., 2020), so that all values, both for historical and projection runs and RCM and GCM simulations are
 216 comparable. A schematic of the process described above is provided in **Fig. S1**.

217 3 Results

218 The October and January precipitation climatologies for the period 1985-2005 are displayed in **Fig. 3** and **Fig. 4**,
 219 respectively. We use October and January climatologies, because these 2 months may be considered representative
 220 of the distinctive processes controlling precipitation over SAF (see section 2.2). We avoid using seasonal means, since
 221 the temporal averaging of precipitation often obscures attributes that are better identified on a monthly level. The
 222 remaining months of the rainy season are shown in the supplementary material. More specifically, we use October as
 223 it is the month that heralds the onset of the rainy season and is often associated with weak precipitation and convective
 224 processes that are mainly due to excess surface heating. Also, it is during October that the most intense formations of
 225 the heat low expression of the AL are observed. Likewise, we use January as it represents the core of the rainy season,

226 with very strong large-scale precipitation, mainly from the southeastern (SE) part of SAF, through transient synoptic
227 scale low pressure systems.

228 As it is displayed in **Fig. 3**, precipitation during October occurs in the northwestern (NW) part and the SE part of SAF.
229 Precipitation in the NW part is associated with the southward migration of the rainband (Nicholson, 2018), while
230 precipitation over the SE part is associated with an early formation of the tropical temperate troughs (TTTs). As it is
231 evident from **Fig. 3**, CCLM4-8-17.v1 reduces precipitation amounts (approximately 4-5 mm/d) in both the NW and
232 SE parts of SAF, relative to the lateral boundary forcing it receives. On the contrary, RCA4.v1 systematically enhances
233 precipitation amounts, regardless of the driving GCM. Also, precipitation according to RCA4.v1 displays a very
234 localized spatial pattern with very strong spatial heterogeneity. This attribute is indicative of specific structural model
235 biases related to how high-resolution elevation affects precipitation in RCA.v1 (Van Vooren et al., 2019). This is
236 particularly evident in the mountainous region over coastal Angola. REMO2009.v1 also enhances precipitation
237 amounts regardless of the driving GCM, however in a much more spatially homogeneous way than RCA4.v1.

238

239 As it is shown in **Fig. 4**, high precipitation amounts during January are observed over the northern and eastern regions
240 of SAF. During January, differences among the driving GCMs become more pronounced, however, all models agree
241 on the dry conditions observed over the southwestern (SW) part of SAF. With regards to the downscaled products,
242 CCLM4-8-17.v1 produces high precipitation amounts over the central part of northern SAF but displays varying
243 amounts of precipitation over the coastal parts, depending on the driving GCM. RCA4.v1 downscale precipitation in
244 a very localized pattern and enhances precipitation over areas with steep terrain. Also, precipitation over the lake
245 Malawi region is particularly enhanced, regardless of the driving GCM. REMO2009.v1 displays similar precipitation
246 amounts to its driving GCMs, however it enhances precipitation over the coastal part of Angola and Mozambique and
247 yields excess precipitation over lake Malawi, when it is driven by HadGEM2-ES and IPSL. The monthly climatologies
248 for the rest of the rainy season months are shown in the supplementary material (**Fig. S2 – S5**).

249

250 In **Fig. 5** the monthly precipitation bias for October over SAF is shown. Biases are calculated using the CHIRPS
251 satellite rainfall product as a reference. With the exception of IPSL-CM5A (LR/MR) and CanESM2, all other GCMs
252 display a consistent wet bias that ranges from 0.1 – 30 mm/d (in isolated areas), with most values over SAF falling
253 0.1-3 mm/d. Overall, the same pattern generally holds for RCA4.v1 and REMO2009.v1, while CCLM4-7-18.v1
254 displays a systematic dry bias that reaches 2 mm/d, when forced with EC-EARTH, MPI-ESM-LR and HadGEM2-ES.
255 More specifically, concerning RCA4.v1, the region where the highest wet bias is observed is over the Angola region
256 and over the NW parts of coastal Angola. The dry bias regions in RCA4.v1 are identified over the northeastern (NE)
257 and southern parts of SAF and they rarely exceed -1.5 mm/d.

258 The monthly precipitation biases for January over SAF are shown in **Fig. 6**. There is a prevailing wet bias identified
259 in almost all GCMs that typically reaches 3 - 3.5 mm/d, however, in MIROC5, NorESM and GFDL-ESM2M the
260 biases exceed 5 mm/d over a major part of SAF. Another feature that systematically appears in GCMs is a dry bias
261 over the NE part of SAF. This bias pattern is also identified in almost all RCMs with a systematic wet bias over central
262 and western SAF and a region of dry bias in the NE part. More specifically, in RCA4.v1 and REMO2009.v1, there is

263 a dry bias over the NE and the southern coast of SAF, while in CCLM4-7-18.v1 the dry bias over the eastern region
264 extends inland to cover almost the whole of Mozambique. Another interesting feature is identified around the Angolan
265 coast, where wet biases exceed 5 mm/d, while over an adjacent region there is a strip of dry biases that reaches 2
266 mm/d. Considering the abrupt increase in elevation and the steep escarpment over the coastal Angola-Namibia region,
267 this is possibly caused by local circulation driving excess moisture transport from the Atlantic Ocean and overly
268 aggressive orographically triggered precipitation on the windward side of the topography (wet bias strip), that leads
269 to dry conditions in the lee side (dry bias strip) (Howard and Washington, 2018). It is noted that the wet bias over the
270 coastal region is identified in most of the RCA4.v1 simulations and in all REMO2009.v1 simulations, however, the
271 dry bias in the lee side is seen in CCLM4-7.18.v1 only. The monthly precipitation biases for the rest of the rainy
272 season months are shown in the supplementary material (**Fig. S6 – S9**). Monthly precipitation biases averaged over
273 southern Africa (SAF-All) and the three subregions examined are displayed in **Fig. S10**.

274

275 A more detailed look into specific subregions over SAF where certain climatological features and processes are at
276 play, can help gain a more in-depth insight of how the precipitation biases are distributed during each month of the
277 rainy season and whether or not the RCMs display any improvement relative to their driving GCMs. For this reason,
278 we plot the RCM increments (RCM-GCM) as a function of the GCM biases (GCM-OBS). The results for October
279 over SAF and the 3 subregions are displayed in **Fig. 7**. In general, all points are identified close to the $y=-x$ line, hence
280 there is a tendency that RCMs systematically counteract GCM biases. There are nonetheless substantial differences
281 between the four regions. For instance, over SAF-All region the IPSL-MR GCM has a wet bias equal to almost 1
282 mm/day, which is counteracted by RCA by an increment of -0.4 mm/month. Other RCA simulations when driven by
283 HadGEM2-ES, CNRM-CM5 or EC-EARTH, display an RCM increment similar to that of the GCM bias, hence RCMs
284 mitigate the GCM bias. Over the Angola region most of the RCMs display an RCM increment that is nearly equal to
285 the GCM bias. Similar conclusions are drawn for Regions C and D also. The RCM increments as a function of the
286 GCM biases for January are shown in **Fig. 8**. For all regions except the SAfr region points are lying closely to the $y=-x$ line,
287 hence overall, RCM increments counteract the GCM biases. The scatterplots for the rest of the months of the
288 rainy season are shown in the supplementary material (**Fig. S11 – S14**). In general, although precipitation in RCMs is
289 strongly dependent on the driving GCMs, the RCM increments are anticorrelated to the GCM biases. The
290 anticorrelations are particularly strong for the Dec-Mar period of the rainy season over SAF-All region, B and C, but
291 not over D (**Fig. S15**).

292 In **Fig. 9** the mean analysis of variance of all RCMs driven by the same GCM and of all GCMs driving the same RCM
293 is shown. Values are spatially averaged for southern Africa and the 3 subregions examined (land pixels only) and refer
294 to the period 1985-2005. In SAF-All region, monthly precipitation during October and November is dominated by the
295 RCMs, while during Jan-Mar, it is the GCMs that play a dominant role in formulating precipitation over SAF. This is
296 indicative of the impact that RCMs exert on the formulation of precipitation during Oct-Nov-Dec and the fact that the
297 contribution from the GCMs becomes dominant during Jan-Feb-Mar. The fact that the contribution of RCMs during
298 Oct-Nov-Dec dominates can be attributed to the fact that precipitation during these months is the result of regional

299 processes that are largely dependent on the coupling between the surface and the atmosphere. The land-atmosphere
300 coupling is a characteristic resolved by the RCMs, through mechanisms described in land surface models, planetary
301 boundary layer schemes, convection schemes etc., making the contribution of the large scale drivers from the GCM
302 less important. However, during Jan-Feb-Mar we observe that the contribution from the RCMs is reduced, and it is
303 the GCMs that control the monthly precipitation variability. This can be attributed to the fact that during Jan-Feb-Mar
304 it is the large-scale circulation that modulates precipitation over SAF and the GCMs control the transient synoptic
305 scale systems that enter SAF. Over the Angola region, the pattern is similar, however, October and November
306 precipitation are closer to the diagonal, indicating an almost equal contribution by both RCMs and GCMs. Also, Dec-
307 Feb move closer to the diagonal, nevertheless, precipitation during March is mainly formulated by GCMs. Over the
308 East Coast region, October remains equally influenced by both RCMs and GCMs, however November and December
309 are dominated by the influence of the RCMs. Over the SAfr region, precipitation for all months except October is
310 influenced by GCMs.

311 In **Fig. 10** the climate change signal for October precipitation over SAF is depicted. All GCMs agree that October
312 precipitation will decline by approximately 2 mm/d over the regions that experience precipitation during this period,
313 namely the NW and SE parts of SAF. In addition, some GCMs display a minor precipitation increase (0 - 0.5 mm/d)
314 in the SW part of SAF, while some others display a slightly larger (1.5 mm/d) precipitation increase over the eastern
315 parts of South Africa. Moreover, it is seen that the precipitation change signal is replicated by almost all the
316 downscaling RCMs, nevertheless, there are some considerable differences between the RCMs and their driving GCM.
317 More specifically, RCA4.v1 in almost all simulations, displays a larger reduction of the precipitation change signal
318 relative to its driving GCM, both in magnitude and in spatial extent. Precipitation changes in CCLM4-8-17.v1 seem
319 to follow closely the driving GCMs, with a severe exception when CNRM-CM5 is used (the NW part of SAF
320 experiences precipitation decline almost 4 mm/d larger than in the driving GCM). The case for when CCLM4-8-17.v1
321 is driven by CNRM-CM5 may be partly caused by the fact that the historical simulation had erroneously used lateral
322 boundary conditions from a different simulation member of CNRM-CM5 (Vautard et al., 2020). In REMO2009.v1, a
323 precipitation decline region is identified in the NW part of SAF and a minor precipitation increase over eastern South
324 Africa is identified. This pattern for REMO2009.v1 appears to be consistent, regardless of the driving GCM, which
325 could be partly explained by the fact that precipitation during October is thermally driven, and thus the impact of the
326 driving GCMs is not dominant. The precipitation increase in the SE part of SAF is seen over a localized region and
327 could be associated with an increase in the precipitation caused by the Tropical Temperate Troughs (TTTs) (Ratna et
328 al., 2013; Macron et al., 2014; Shongwe et al., 2015).

329 In **Fig. 11** the climate change signal for precipitation during January is displayed. The precipitation change displays a
330 very strong regional heterogeneity. It is also observed that although there is a strong precipitation change signal in all
331 driving GCMs, not all RCMs downscale the signal uniformly. It is also notable that, even among the GCMs, there are
332 substantial differences in the spatial extent and sign of the change. Nevertheless, there are some features that appear
333 in most of the simulations. For instance, almost all GCMs project drying conditions over the SW part of SAF,
334 especially the coastal zone. The precipitation decline is equal to -1 mm/d. This could be explained by a consistent

335 increase in frequency of the Benguela Coastal Low-Level Jet events (Lima et al., 2019; Reboita et al., 2019), causing
336 oceanic upwelling and a subsequent reduction in precipitation. In addition, there is a subset of GCMs that identify a
337 severe precipitation decline over the Angola region that reaches -5 mm/d. Furthermore, in many GCMs a region of
338 precipitation increase is identified, extending from central SAF towards SE SAF. This is particularly identifiable in
339 HadGEM2-ES, and the RCM simulations forced by it. The monthly precipitation changes for the rest of the rainy
340 season months is shown in the supplementary material (**Fig. S16 – S19**).

341 In **Fig. 12** the spatial average of the $RCM_{DRI} - DRI$ difference (DIFF) is shown for the whole of SAF (land pixels
342 only). If $DIFF > 0$, it indicates that the RCMs enhance precipitation relative to their driving GCM, while if $DIFF < 0$
343 then RCMs reduce precipitation relative to their driving GCM. As it is shown, DIFF values for October are symmetric
344 around zero and do not exceed the range (-1) – 1 mm/d, either for the historical or the future period. Almost symmetric
345 are the DIFF values for November also, however, their spread increases, reaching values that range (-2) – 2 mm/d. In
346 both months, CCLM4-7-18.v1 always reduces precipitation amounts relative to the lateral boundary forcing it
347 receives, regardless of the driving GCM or the period examined. During December, the precipitation reduction in all
348 RCMs becomes more pronounced and reaches values equal to -3 mm/d. In January, only 1 RCM enhances
349 precipitation (~0.5 mm/d) with all the rest displaying precipitation reduction. During February and March, some
350 positive DIFF values re-appear for some simulations. Overall, there is a strong linear relationship between DIFF in
351 1985-2005 and 2065-2095, which further implies that if an RCM is drier than its driving GCM during the historical
352 period, then it will retain this attribute during the future period also. Nonetheless, we highlight that RCMs preserve
353 precipitation change signal generated by the GCMs. Considering that one primary shortcoming of the GCMs over
354 SAF is their wet bias and that RCMs systematically reduce this bias, we gain increased confidence that RCMs can be
355 reliably used for future projections with regards to precipitation change.

356 In **Fig. 13** the spatial average of the precipitation change signal from RCMs and their driving GCMs relative to 1985-
357 2005 for SAF and the 3 subregions is displayed. Concerning SAF-All region, all models during October identify a
358 precipitation reduction at the end of the 21st century that can reach -0.9 mm/d. The precipitation decline signal is also
359 identified during November, indicating a later onset of the rainy season over SAF, as it has already been shown for
360 CMIP5 (Dunning et al., 2018). During December and January there is a variability in the spatial averages of the change
361 signal that ranges from -0.8 to 0.8 mm/d. A similar pattern is also seen for February and March. The distribution of
362 the ensemble members for both RCMs and GCMs in Regions B and C is similar to that of SAF-All region, however
363 in Regions B and C precipitation change values display a considerably larger spread. Over the SAfr region the climate
364 change signal is symmetric around 0 for all months, except March.

365 The impact the RCMs and GCMs on monthly precipitation for the period 2065-2095 under RCP8.5 is shown in **Fig.**
366 **14**. Regions A and B show a similar behavior as in the historical period (**Fig. 9**), however, over the East Coast region,
367 precipitation during March is more strongly dominated by GCMs. The same observation holds also over the SAfr
368 region. In general, regional processes continue to dominate contributions to variability during Oct-Nov, while large
369 scale features dominate during Dec-Mar.

370

371 **3 Discussion and conclusions**

372 In this work we investigate whether it is the RCMs or the driving GCMs that control the monthly precipitation
373 variability, monthly precipitation biases and the climate change signal over southern Africa and how these
374 relationships vary from month-to-month throughout the rainy season. Our work examines monthly precipitation
375 variance caused by the lateral boundary conditions and does not examine parameter and structural uncertainty
376 separately in the multi-RCM and the multi-GCM ensembles analyzed. More specifically, we use an ensemble of 19
377 RCM simulations performed in the context of CORDEX-Africa and their driving GCMs. According to the literature
378 (Munday and Washington, 2018), precipitation in the CMIP5 simulations is characterized by a systematic wet bias
379 over southern Africa. In the CORDEX-Africa RCM simulations there is also a persistent wet bias, especially during
380 the core of the rainy season (DJF), however, it is of smaller magnitude and of smaller spatial extent.. It is found that
381 all RCMs reduce monthly precipitation compared to their driving GCMs for both historical (1985-2005) and future
382 period (2065-2095) under RCP8.5.

383 The Angola region, which encompasses the activity of the Angola Low pressure system, displays the highest wet
384 biases with regards to mean monthly precipitation, among all subregions examined. The months with the largest wet
385 biases (for the Angola region) is found to be November, while the month with the largest precipitation bias spread is
386 found to be March. In all months except of October, the CMIP5 GCMs display biases that are approximately 1-1.5
387 mm/d wetter than the wettest CORDEX-Africa RCM ensemble members. Over the East Coast region, representing
388 the wider area over Mozambique, the bias signal is reversed after January, with most of the RCMs displaying a dry
389 bias. Over the SAfr region, the majority of models display a consistent wet bias for all months of the rainy season. All
390 models (CMIP5 and CORDEX-Africa) display an intense dry bias in the NE part of SAF, which can be related to the
391 misrepresentation of the moisture transport entering the region from the Indian Ocean (Munday and Washington,
392 2018). In general, although RCMs display an improvement of precipitation biases relative to their driving GCMs, still
393 some bias patterns persist even in RCMs, calling for a process-based evaluation of specific climatological features
394 such as the formulation of the Angola Low and the transport of moisture from the NE part of SAF towards central
395 SAF.

396 More specifically, we found that CCLM4-7-18.v1 produces the smallest bias when the whole of SAF is examined,
397 however, it displays a systematic dry bias over the East Coast region (greater Mozambique region), hence, CCLM4-
398 7-18.v1 should be used with caution over eastern SAF, especially if it is exploited within drought-related climate
399 services. Concerning RCA4.v1, we find a very regionally heterogeneous -almost pixelated- spatial pattern for
400 precipitation, which can be attributed to the sharp topography used (Van Vooren et al., 2019). RCA4.v1, due to the
401 large size of its ensemble, is optimal for analyzing its behavior under different driving GCMs. In general, we find that
402 RCA4.v1 is more prone to follow the signal received from the driving GCMs, contrary to what is observed for
403 CCLM4-7-18.v1. REMO2009.v1 presents a compromise between the behaviors of RCA4.v1 and CCLM4-7-18.v1.
404 It is highly recommended that when RCM simulations are used for the whole of SAF or a subregion thereof, the spread
405 and statistical properties of all available RCMs and their driving GCMs should be examined and an ensemble of RCMs
406 should be employed based on their ability to reproduce key climatic features of the region of interest. Increasing

407 evidence is provided that not all models are fit for constructing an ensemble mean (or median) for all regions (Her et
408 al., 2019; Raju and Kumar, 2020; Tebaldi and Knutti, 2007). Lastly, a very important aspect when the calculation and
409 characterization of biases is discussed for GCMs and RCMs, is that biases are assessed based on a satellite or gauge-
410 based product, which are often erroneously regarded as “the ground truth” (Harrison et al., 2019; Alexander et al.,
411 2020). Of course, the climate community is bound to work with the state-of-the-science products that are available,
412 however, biases and errors in the “observational datasets” should be kept in mind when the bias of climate models is
413 discussed. In this work we use the CHIRPS precipitation product, as it has been shown to outperform other satellite
414 precipitation products (Toté et al., 2015; Ayehu et al., 2018; Dinku et al., 2018).

415 Concerning the climate change signal, there is a strong agreement among all GCMs and RCMs that precipitation
416 during October will decrease by $(-0.1) - (-1)$ mm/d, a fact associated with a projected later onset of the rainy season,
417 which is further linked with a northward shift of the tropical rain belt (Dunning et al., 2018; Lazenby et al., 2018).
418 The topic of reduced early rainfall over southern Africa for the end of the 21st century under all emission
419 scenarios/pathways has been examined extensively for the CMIP3 and CMIP5 GCM ensembles (Seth et al., 2011;
420 Cook and Vizy, 2021; Lazenby et al., 2018; Howard and Washington, 2019). A common observation in all CMIP5
421 GCMs for the early rainy season by the end of the 21st century is that instability over southern Africa reduces, surface
422 temperature increases, and the heat low phase of the Angola Low pressure system is strengthened (Howard and
423 Washington, 2019). However, rainfall decline in the CMIP5 ensemble over southern Africa should be additionally
424 considered in the context of the systematic precipitation biases already diagnosed in the historical simulations
425 (Munday and Washington, 2018; Howard and Washington, 2019). Considering that the systematic wet precipitation
426 bias is significantly reduced in the CORDEX-Africa ensemble relative to their driving CMIP5 GCMs (Karypidou et
427 al., 2022), we gain confidence that future precipitation projections according to the CORDEX-Africa ensemble
428 provide a more plausible future scenario. For the rest of the months, the results are variable, indicating the need for a
429 multi-model approach, when climate change impacts are assessed. A feature that is identified in some GCMs and is
430 transferred to the downscaling RCMs, is a precipitation increase that extends from the central SAF region towards the
431 southeast. This result is consistent with previous work that shows an increase in frequency of landfalling cyclones
432 along the eastern seaboard of SAF (Muthige et al., 2018). Since tropical cyclones are a particular cause of severe
433 flooding events over the region of Mozambique, there is an urgent need for planning and mitigation strategies over
434 the region.

435 Concerning precipitation variability and whether it is the RCMs or the driving GCMs that dominate monthly
436 precipitation, we find that, as expected, over the whole of SAF (SAF-All region), October and November are
437 dominated by RCMs, while during Dec-Mar it is the GCMs that mainly formulate the precipitation climatologies. This
438 is explained by the fact that after December there is a strong large-scale forcing, which is provided to the RCMs by
439 the lateral boundary conditions given through the GCMs. The results for the historical period are comparable to that
440 for future projections.

441 Lastly, it is imperative to highlight that the impact of the lateral boundary conditions on RCM simulations comprise
442 only a portion of the potential sources of uncertainty in the CORDEX-Africa ensemble examined, therefore attributing
443 entirely the variance of RCM simulations to the driving GCMs would be erroneous. Therefore, we mention that

444 uncertainty in RCM simulations can have a plethora of sources that are mainly categorized as parameter or structural
445 uncertainty (Günther et al., 2020; Howland et al., 2022). These types of uncertainty sources may relate to the
446 parameterization schemes employed by each RCM or assumptions and numerical choices involved in the dynamics
447 of each specific RCM. However, since within CORDEX-Africa only a limited number of variables is being made
448 available to the community, it would be impossible to meticulously comment on all possible sources of uncertainty
449 and access the impact of their variance on monthly precipitation.

450 *Code and data availability*

451 For the data processing and statistical analysis we used the R Project for Statistical Computing (<https://www.r-project.org/>), the Climate Data Operators (CDO) (<https://code.mpimet.mpg.de/projects/cdo/>) and Bash programming
452 routines. Processing scripts are available via ZENODO under DOI: <https://doi.org/10.5281/zenodo.5569984>. CMIP5
453 and CORDEX-Africa precipitation data were retrieved from the Earth System Grid Federation (ESGF) portal
454 (<https://esgf-data.dkrz.de/projects/esgf-dkrz/>). The Climate Hazards Group InfraRed Precipitation with Station data
455 (CHIRPS) products were retrieved from: <https://www.chc.ucsb.edu/data/chirps>.

456

458 *Supplement*

459 The supplement related to this article is available online.

460

461 *Author contribution*

462 MCK, SPS and EK designed the research. MCK performed the analysis and prepared the manuscript. SPS, EK, LS
463 and GN edited the manuscript and provided corrections.

464

465 *Competing interests*

466 The authors declare that they have no competing interests.

467

468 *Acknowledgements*

469 This article is funded by the AfriCultuReS project "Enhancing Food Security in African Agricultural Systems with
470 the Support of Remote Sensing", (European Union's Horizon 2020 Research and Innovation Framework Programme
471 under grant agreement No. 774652). The authors would like to thank the Scientific Support Centre of the Aristotle
472 University of Thessaloniki (Greece) for providing computational/storage infrastructure and technical support. MCK
473 was funded by the Hellenic Foundation for Research & Innovations, under the 2nd Call for PhD Candidates (application
474 No. 1323).

475

476 **References**

477 Abiodun, B.J., Makhanya, N., Petja, B., Abatan, A.A., Oguntunde, P.G., 2019. Future projection of droughts over major river
478 basins in Southern Africa at specific global warming levels. *Theor. Appl. Climatol.* 137, 1785–1799.
479 <https://doi.org/10.1007/s00704-018-2693-0>

480 Alexander, L.V., Bador, M., Roca, R., Contractor, S., Donat, M.G., Nguyen, P.L., 2020. Intercomparison of annual precipitation
481 indices and extremes over global land areas from in situ, space-based and reanalysis products. *Environ. Res. Lett.* 15,
482 055002. <https://doi.org/10.1088/1748-9326/ab79e2>

483 Bentsen, M., Bethke, I., Debernard, J.B., Iversen, T., Kirkevåg, A., Seland, Ø., Drange, H., Roelandt, C., Seierstad, I.A., Hoose,
484 C., Kristjánsson, J.E., 2013. The Norwegian Earth System Model, NorESM1-M – Part 1: Description and basic evaluation
485 of the physical climate. *Geosci. Model Dev.* 6, 687–720. <https://doi.org/10.5194/gmd-6-687-2013>

486 Boberg, F., Christensen, J.H., 2012. Overestimation of Mediterranean summer temperature projections due to model deficiencies.
487 *Nat. Clim. Change* 2, 433–436. <https://doi.org/10.1038/nclimate1454>

488 Casale, M., Drimie, S., Quinlan, T., Ziervogel, G., 2010. Understanding vulnerability in southern Africa: comparative findings
489 using a multiple-stressor approach in South Africa and Malawi. *Reg. Environ. Change* 10, 157–168.
490 <https://doi.org/10.1007/s10113-009-0103-y>

491 CCCma, 2017. Environment and Climate Change Canada - Climate Change - CanESM2 [WWW Document]. URL
492 <http://www.ec.gc.ca/ccmac-ccma/default.asp?lang=En&xml=1A3B7DF1-99BB-4EC8-B129-09F83E72D645>
493 (accessed 6.23.20).

494 Christensen, O.B., Kjellström, E., 2020. Partitioning uncertainty components of mean climate and climate change in a large
495 ensemble of European regional climate model projections. *Clim. Dyn.* 54, 4293–4308. <https://doi.org/10.1007/s00382-020-05229-y>

496 Collins, W.J., Bellouin, N., Doutriaux-Boucher, M., Gedney, N., Halloran, P., Hinton, T., Hughes, J., Jones, C.D., Joshi, M.,
497 Liddicoat, S., Martin, G., O'Connor, F., Rae, J., Senior, C., Sitch, S., Totterdell, I., Wiltshire, A., Woodward, S., 2011.
498 Development and evaluation of an Earth-System model – HadGEM2. *Geosci. Model Dev.* 4, 1051–1075.
499 <https://doi.org/10.5194/gmd-4-1051-2011>

500 Conway, D., van Garderen, E.A., Deryng, D., Dorling, S., Krueger, T., Landman, W., Lankford, B., Lebek, K., Osborn, T., Ringler,
501 C., Thurlow, J., Zhu, T., Dalin, C., 2015. Climate and southern Africa's water–energy–food nexus. *Nat. Clim. Change* 5,
502 837–846. <https://doi.org/10.1038/nclimate2735>

503 Crétat, J., Pohl, B., Dieppois, B., Berthou, S., Pergaud, J., 2019. The Angola Low: relationship with southern African rainfall and
504 ENSO. *Clim. Dyn.* 52, 1783–1803. <https://doi.org/10.1007/s00382-018-4222-3>

505 Déqué, M., Rowell, D.P., Lüthi, D., Giorgi, F., Christensen, J.H., Rockel, B., Jacob, D., Kjellström, E., de Castro, M., van den
506 Hurk, B., 2007. An intercomparison of regional climate simulations for Europe: assessing uncertainties in model
507 projections. *Clim. Change* 81, 53–70. <https://doi.org/10.1007/s10584-006-9228-x>

508 Déqué, M., Somot, S., Sanchez-Gomez, E., Goodess, C.M., Jacob, D., Lenderink, G., Christensen, O.B., 2012. The spread amongst
509 ENSEMBLES regional scenarios: regional climate models, driving general circulation models and interannual
510 variability. *Clim. Dyn.* 38, 951–964. <https://doi.org/10.1007/s00382-011-1053-x>

511 Dinku, T., Funk, C., Peterson, P., Maidment, R., Tadesse, T., Gadaïn, H., Ceccato, P., 2018. Validation of the CHIRPS satellite
512 rainfall estimates over eastern Africa. *Q. J. R. Meteorol. Soc.* 144, 292–312. <https://doi.org/10.1002/qj.3244>

513 Di Luca, A., de Elía, R., Laprise, R., 2013. Potential for added value in temperature simulated by high-resolution nested RCMs in
514 present climate and in the climate change signal. *Clim. Dyn.* 40, 443–464. <https://doi.org/10.1007/s00382-012-1384-2>

515 Diffenbaugh, N.S., Giorgi, F., 2012. Climate change hotspots in the CMIP5 global climate model ensemble. *Clim. Change* 114,
516 813–822. <https://doi.org/10.1007/s10584-012-0570-x>

517 Dosio, A., Jones, R.G., Jack, C., Lennard, C., Nikulin, G., Hewitson, B., 2019. What can we know about future precipitation in
518 Africa? Robustness, significance and added value of projections from a large ensemble of regional climate models. *Clim.
519 Dyn.* 53, 5833–5858. <https://doi.org/10.1007/s00382-019-04900-3>

520 Dufresne, J.-L., Foujols, M.-A., Denvil, S., Caubel, A., Marti, O., Aumont, O., Balkanski, Y., Bekki, S., Bellenger, H., Benshila,
521 R., Bony, S., Bopp, L., Braconnot, P., Brockmann, P., Cadule, P., Cheruy, F., Codron, F., Cozic, A., Cugnet, D., de
522 Noblet, N., Duvel, J.-P., Ethé, C., Fairhead, L., Fichefet, T., Flavoni, S., Friedlingstein, P., Grandpeix, J.-Y., Guez, L.,
523 Guiyardi, E., Hauglustaine, D., Hourdin, F., Idelkadi, A., Ghantas, J., Joussaume, S., Kageyama, M., Krinner, G.,
524 Labetoulle, S., Lahellec, A., Lefebvre, M.-P., Lefevre, F., Levy, C., Li, Z.X., Lloyd, J., Lott, F., Madec, G., Mancip, M.,
525 Marchand, M., Masson, S., Meurdesoif, Y., Mignot, J., Musat, I., Parouty, S., Polcher, J., Rio, C., Schulz, M.,
526 Swingedouw, D., Szopa, S., Talandier, C., Terray, P., Viovy, N., Vuichard, N., 2013. Climate change projections using
527 the IPSL-CM5 Earth System Model: from CMIP3 to CMIP5. *Clim. Dyn.* 40, 2123–2165. <https://doi.org/10.1007/s00382-012-1636-1>

528 Dunne, J.P., John, J.G., Adcroft, A.J., Griffies, S.M., Hallberg, R.W., Shevliakova, E., Stouffer, R.J., Cooke, W., Dunne, K.A.,
529 Harrison, M.J., Krasting, J.P., Malyshev, S.L., Milly, P.C.D., Phillipps, P.J., Sentman, L.T., Samuels, B.L., Spelman,
530 M.J., Winton, M., Wittenberg, A.T., Zadeh, N., 2012. GFDL's ESM2 Global Coupled Climate–Carbon Earth System
531 Models. Part I: Physical Formulation and Baseline Simulation Characteristics. *J. Clim.* 25, 6646–6665.
532 <https://doi.org/10.1175/JCLI-D-11-00560.1>

533 Dunning, C.M., Black, E., Allan, R.P., 2018. Later Wet Seasons with More Intense Rainfall over Africa under Future Climate
534 Change. *J. Clim.* 31, 9719–9738. <https://doi.org/10.1175/JCLI-D-18-0102.1>

537 Funk, C., Peterson, P., Landsfeld, M., Pedreros, D., Verdin, J., Shukla, S., Husak, G., Rowland, J., Harrison, L., Hoell, A.,
 538 Michaelsen, J., 2015. The climate hazards infrared precipitation with stations—a new environmental record for
 539 monitoring extremes. *Sci. Data* 2, 150066. <https://doi.org/10.1038/sdata.2015.66>

540 Giorgi, M.A., Jungclaus, J., Reick, C.H., Legutke, S., Bader, J., Böttiger, M., Brovkin, V., Crueger, T., Esch, M., Fieg, K.,
 541 Glushak, K., Gayler, V., Haak, H., Hollweg, H.-D., Ilyina, T., Kinne, S., Kornblueh, L., Matei, D., Mauritzen, T.,
 542 Mikolajewicz, U., Mueller, W., Notz, D., Pithan, F., Raddatz, T., Rast, S., Redler, R., Roeckner, E., Schmidt, H., Schnur,
 543 R., Segschneider, J., Six, K.D., Stockhouse, M., Timmreck, C., Wegner, J., Widmann, H., Wieners, K.-H., Claussen, M.,
 544 Marotzke, J., Stevens, B., 2013. Climate and carbon cycle changes from 1850 to 2100 in MPI-ESM simulations for the
 545 Coupled Model Intercomparison Project phase 5. *J. Adv. Model. Earth Syst.* 5, 572–597.
 546 <https://doi.org/10.1002/jame.20038>

547 Giorgi, F., Gutowski, W.J., 2015. Regional Dynamical Downscaling and the CORDEX Initiative. *Annu. Rev. Environ. Resour.* 40,
 548 467–490. <https://doi.org/10.1146/annurev-environ-102014-021217>

549 Harrison, L., Funk, C., Peterson, P., 2019. Identifying changing precipitation extremes in Sub-Saharan Africa with gauge and
 550 satellite products. *Environ. Res. Lett.* 14, 085007. <https://doi.org/10.1088/1748-9326/ab2cae>

551 Hazeleger, W., Severijns, C., Semmler, T., Štefánská, S., Yang, S., Wang, X., Wyser, K., Dutra, E., Baldasano, J.M., Bintanja,
 552 R., Bougeault, P., Caballero, R., Ekman, A.M.L., Christensen, J.H., van den Hurk, B., Jimenez, P., Jones, C., Källberg,
 553 P., Koenigk, T., McGrath, R., Miranda, P., van Noije, T., Palmer, T., Parodi, J.A., Schmitt, T., Selten, F., Storelvmo, T.,
 554 Sterl, A., Tapamo, H., Vancoppenolle, M., Viterbo, P., Willén, U., 2010. EC-EarthA Seamless Earth-System Prediction
 555 Approach in Action. *Bull. Am. Meteorol. Soc.* 91, 1357–1364. <https://doi.org/10.1175/2010BAMS2877.1>

556 Her, Y., Yoo, S.-H., Cho, J., Hwang, S., Jeong, J., Seong, C., 2019. Uncertainty in hydrological analysis of climate change: multi-
 557 parameter vs. multi-GCM ensemble predictions. *Sci. Rep.* 9, 4974. <https://doi.org/10.1038/s41598-019-41334-7>

558 Howard, E., Washington, R., 2018. Characterizing the Synoptic Expression of the Angola Low. *J. Clim.* 31, 7147–7165.
 559 <https://doi.org/10.1175/JCLI-D-18-0017.1>

560 IPCC, Stocker, T.F., 2013. Climate Change 2013: The Physical Science Basis. Cambridge University Press.

561 Jeffrey, S., Rotstayn, L.D., Collier, M., Dravitzki, S.M., Hamalainen, C., Moeseneder, C., Wong, K., Syktus, J., 2013. Australia's
 562 CMIP 5 submission using the CSIRO-Mk 3.6 model.

563 Kerkhoff, C., Künsch, H.R., Schär, C., 2015. A Bayesian Hierarchical Model for Heterogeneous RCM–GCM Multimodel
 564 Ensembles. *J. Clim.* 28, 6249–6266. <https://doi.org/10.1175/JCLI-D-14-00606.1>

565 Lima, D.C.A., Soares, P.M.M., Semedo, A., Cardoso, R.M., Cabos, W., Sein, D.V., 2019. How Will a Warming Climate Affect
 566 the Benguela Coastal Low-Level Wind Jet? *J. Geophys. Res. Atmospheres* 124, 5010–5028.
 567 <https://doi.org/10.1029/2018JD029574>

568 Luan, Y., Cui, X., Ferrat, M., 2013. Historical trends of food self-sufficiency in Africa. *Food Secur.* 5, 393–405.
 569 <https://doi.org/10.1007/s12571-013-0260-1>

570 Lyon, B., Mason, S.J., 2007. The 1997–98 Summer Rainfall Season in Southern Africa. Part I: Observations. *J. Clim.* 20, 5134–
 571 5148. <https://doi.org/10.1175/JCLI4225.1>

572 Masipa, T.S., 2017. The impact of climate change on food security in South Africa: Current realities and challenges ahead. *Jàmbá J. Disaster Risk Stud.* 9. <https://doi.org/10.4102/jamba.v9i1.411>

573 Maíre, G., Pinto, I., Ndebele-Murisa, M., Muthighe, M., Lennard, C., Nikulin, G., Dosio, A., Meque, A., 2018. The southern African
 574 climate under 1.5°C and 2°C of global warming as simulated by CORDEX regional
 575 climate models. *Environ. Res. Lett.* 13, 065002. <https://doi.org/10.1088/1748-9326/aab190>

576 Misselhorn, A., Hendriks, S.L., 2017. A systematic review of sub-national food insecurity research in South Africa: Missed
 577 opportunities for policy insights. *PLOS ONE* 12, e0182399. <https://doi.org/10.1371/journal.pone.0182399>

578 Munday, C., Washington, R., 2018. Systematic Climate Model Rainfall Biases over Southern Africa: Links to Moisture Circulation
 579 and Topography. *J. Clim.* 31, 7533–7548. <https://doi.org/10.1175/JCLI-D-18-0008.1>

580 Munday, C., Washington, R., 2017. Circulation controls on southern African precipitation in coupled models: The role of the
 581 Angola Low. *J. Geophys. Res. Atmospheres* 122, 861–877. <https://doi.org/10.1002/2016JD025736>

582 Muthighe, M.S., Malherbe, J., Englebrecht, F.A., Grab, S., Beraki, A., Maisha, T.R., Merwe, J.V. der, 2018. Projected changes in
 583 tropical cyclones over the South West Indian Ocean under different extents of global warming. *Environ. Res. Lett.* 13,
 584 065019. <https://doi.org/10.1088/1748-9326/aabc60>

585 Nicholson, S.E., 2018. The ITCZ and the Seasonal Cycle over Equatorial Africa. *Bull. Am. Meteorol. Soc.* 99, 337–348.
 586 <https://doi.org/10.1175/BAMS-D-16-0287.1>

587 Nikulin, G., Jones, C., Giorgi, F., Asrar, G., Büchner, M., Cerezo-Mota, R., Christensen, O.B., Déqué, M., Fernandez, J., Hänsler,
 588 A., van Meijgaard, E., Samuelsson, P., Sylla, M.B., Sushama, L., 2012. Precipitation Climatology in an Ensemble of
 589 CORDEX-Africa Regional Climate Simulations. *J. Clim.* 25, 6057–6078. <https://doi.org/10.1175/JCLI-D-11-00375.1>

590 Pinto, I., Jack, C., Hewitson, B., 2018. Process-based model evaluation and projections over southern Africa from Coordinated
 591 Regional Climate Downscaling Experiment and Coupled Model Intercomparison Project Phase 5 models. *Int. J. Climatol.*
 592 38, 4251–4261. <https://doi.org/10.1002/joc.5666>

593 Pinto, I., Lennard, C., Tadross, M., Hewitson, B., Dosio, A., Nikulin, G., Panitz, H.-J., Shongwe, M.E., 2016. Evaluation and
 594 projections of extreme precipitation over southern Africa from two CORDEX models. *Clim. Change* 135, 655–668.
 595 <https://doi.org/10.1007/s10584-015-1573-1>

596 Raju, K.S., Kumar, D.N., 2020. Review of approaches for selection and ensembling of GCMs. *J. Water Clim. Change* 11, 577–
 597 599. <https://doi.org/10.2166/wcc.2020.128>

599 Reason, C.J.C., Jagadheesha, D., 2005. A model investigation of recent ENSO impacts over southern Africa. *Meteorol.*
 600 *Atmospheric Phys.* 89, 181–205. <https://doi.org/10.1007/s00703-005-0128-9>

601 Reboita, M.S., Ambrizzi, T., Silva, B.A., Pinheiro, R.F., da Rocha, R.P., 2019. The South Atlantic Subtropical Anticyclone: Present
 602 and Future Climate. *Front. Earth Sci.* 0. <https://doi.org/10.3389/feart.2019.00008>

603 Shew, A.M., Tack, J.B., Nalley, L.L., Chaminuka, P., 2020. Yield reduction under climate warming varies among wheat cultivars
 604 in South Africa. *Nat. Commun.* 11, 4408. <https://doi.org/10.1038/s41467-020-18317-8>

605 Sillmann, J., Kharin, V.V., Zwiers, F.W., Zhang, X., Bronaugh, D., 2013. Climate extremes indices in the CMIP5 multimodel
 606 ensemble: Part 2. Future climate projections. *J. Geophys. Res. Atmospheres* 118, 2473–2493.
 607 <https://doi.org/10.1002/jgrd.50188>

608 Sørland, S.L., Schär, C., Lüthi, D., Kjellström, E., 2018. Bias patterns and climate change signals in GCM-RCM model chains.
 609 *Environ. Res. Lett.* 13, 074017. <https://doi.org/10.1088/1748-9326/aacc77>

610 Taylor, K.E., Stouffer, R.J., Meehl, G.A., 2012. An Overview of CMIP5 and the Experiment Design. *Bull. Am. Meteorol. Soc.* 93,
 611 485–498. <https://doi.org/10.1175/BAMS-D-11-00094.1>

612 Tebaldi, C., Knutti, R., 2007. The use of the multi-model ensemble in probabilistic climate projections. *Philos. Trans. R. Soc. Math.*
 613 *Phys. Eng. Sci.* 365, 2053–2075. <https://doi.org/10.1098/rsta.2007.2076>

614 Vautard, R., Kadygrov, N., Iles, C., Boberg, F., Buonomo, E., Bülow, K., Coppola, E., Corre, L., Meijgaard, E. van, Nogherotto,
 615 R., Sandstad, M., Schwingshakl, C., Somot, S., Aalbers, E., Christensen, O.B., Ciarlò, J.M., Demory, M.-E., Giorgi, F.,
 616 Jacob, D., Jones, R.G., Keuler, K., Kjellström, E., Lenderink, G., Levavasseur, G., Nikulin, G., Sillmann, J., Solidoro,
 617 C., Sørland, S.L., Steger, C., Teichmann, C., Warrach-Sagi, K., Wulfmeyer, V., 2020. Evaluation of the large EURO-
 618 CORDEX regional climate model ensemble. *J. Geophys. Res. Atmospheres* n/a, e2019JD032344.
 619 <https://doi.org/10.1029/2019JD032344>

620 Voldoire, A., Sanchez-Gomez, E., Salas y Mélia, D., Decharme, B., Cassou, C., Sénési, S., Valcke, S., Beau, I., Alias, A.,
 621 Chevallier, M., Déqué, M., Deshayes, J., Douville, H., Fernandez, E., Madec, G., Maisonnave, E., Moine, M.-P., Planton,
 622 S., Saint-Martin, D., Szopa, S., Tyteca, S., Alkama, R., Belamari, S., Braun, A., Coquart, L., Chauvin, F., 2013. The
 623 CNRM-CM5.1 global climate model: description and basic evaluation. *Clim. Dyn.* 40, 2091–2121.
 624 <https://doi.org/10.1007/s00382-011-1259-y>

625 Watanabe, M., Suzuki, T., O’ishi, R., Komuro, Y., Watanabe, S., Emori, S., Takemura, T., Chikira, M., Ogura, T., Sekiguchi, M.,
 626 Takata, K., Yamazaki, D., Yokohata, T., Nozawa, T., Hasumi, H., Tatebe, H., Kimoto, M., 2010. Improved Climate
 627 Simulation by MIROC5: Mean States, Variability, and Climate Sensitivity. *J. Clim.* 23, 6312–6335.
 628 <https://doi.org/10.1175/2010JCLI3679.1>

629 Wolski, P., Lobell, D., Stone, D., Pinto, I., Crespo, O., Johnston, P., 2020. On the role of anthropogenic climate change in the
 630 emerging food crisis in southern Africa in the 2019–2020 growing season. *Glob. Change Biol.* 26, 2729–2730.
 631 <https://doi.org/10.1111/gcb.15047>

632 Wu, J., Gao, X., 2020. Present day bias and future change signal of temperature over China in a series of multi-GCM driven RCM
 633 simulations. *Clim. Dyn.* 54, 1113–1130. <https://doi.org/10.1007/s00382-019-05047-x>

634 Ayehu, G.T., Tadesse, T., Gessesse, B., Dinku, T., 2018. Validation of new satellite rainfall products over the Upper Blue Nile Basin, Ethiopia.
 635 *Atmospheric Meas. Tech.* 11, 1921–1936. <https://doi.org/10.5194/amt-11-1921-2018>

636 Giorgi, F., Gutowski, W.J., 2015. Regional Dynamical Downscaling and the CORDEX Initiative. *Annu. Rev. Environ. Resour.* 40,
 637 467–490. <https://doi.org/10.1146/annurev-environ-102014-021217>

638 Lloyd, E.A., Bukovsky, M., Mearns, L.O., 2020. An analysis of the disagreement about added value by regional climate models.
 639 *Synthese.* <https://doi.org/10.1007/s11229-020-02821-x>

640 Luca, A.D., Argüeso, D., Evans, J.P., Elía, R. de, Laprise, R., 2016. Quantifying the overall added value of dynamical downscaling
 641 and the contribution from different spatial scales. *J. Geophys. Res. Atmospheres* 121, 1575–1590.
 642 <https://doi.org/10.1002/2015JD024009>

643 Macrón, C., Pohl, B., Richard, Y., Bessafi, M., 2014. How do Tropical Temperate Troughs Form and Develop over Southern
 644 Africa? *J. Clim.* 27, 1633–1647. <https://doi.org/10.1175/JCLI-D-13-00175.1>

645 Nikulin, G., Jones, C., Giorgi, F., Asrar, G., Büchner, M., Cerezo-Mota, R., Christensen, O.B., Déqué, M., Fernandez, J., Hänsler,
 646 A., van Meijgaard, E., Samuelsson, P., Sylla, M.B., Sushama, L., 2012. Precipitation Climatology in an Ensemble of
 647 CORDEX-Africa Regional Climate Simulations. *J. Clim.* 25, 6057–6078. <https://doi.org/10.1175/JCLI-D-11-00375.1>

648 Rana, A., Nikulin, G., Kjellström, E., Strandberg, G., Kupiainen, M., Hansson, U., Kolax, M., 2020. Contrasting regional and
 649 global climate simulations over South Asia. *Clim. Dyn.* 54, 2883–2901. <https://doi.org/10.1007/s00382-020-05146-0>

650 Ratna, S.B., Behera, S., Ratnam, J.V., Takahashi, K., Yamagata, T., 2013. An index for tropical temperate troughs over southern
 651 Africa. *Clim. Dyn.* 41, 421–441. <https://doi.org/10.1007/s00382-012-1540-8>

652 Shongwe, M.E., Lennard, C., Liebmann, B., Kalognomou, E.-A., Ntsangwane, L., Pinto, I., 2015. An evaluation of CORDEX
 653 regional climate models in simulating precipitation over Southern Africa. *Atmospheric Sci. Lett.* 16, 199–207.
 654 <https://doi.org/10.1002/asl2.538>

655 Sørland, S.L., Schär, C., Lüthi, D., Kjellström, E., 2018. Bias patterns and climate change signals in GCM-RCM model chains.
 656 *Environ. Res. Lett.* 13, 074017. <https://doi.org/10.1088/1748-9326/aacc77>

657 Toté, C., Patricio, D., Boogaard, H., Van der Wijngaart, R., Tarnavsky, E., Funk, C., 2015. Evaluation of Satellite Rainfall Estimates
 658 for Drought and Flood Monitoring in Mozambique. *Remote Sens.* 7, 1758–1776. <https://doi.org/10.3390/rs70201758>

659 Van Vooren, S., Van Schaeybroeck, B., Nyssen, J., Van Ginderachter, M., Termonia, P., 2019. Evaluation of CORDEX rainfall in
660 northwest Ethiopia: Sensitivity to the model representation of the orography. *Int. J. Climatol.* 39, 2569–2586.
661 <https://doi.org/10.1002/joc.5971>

662 Vautard, R., Kadygrov, N., Iles, C., Boberg, F., Buonomo, E., Bülow, K., Coppola, E., Corre, L., Meijgaard, E. van, Nogherotto,
663 R., Sandstad, M., Schwingshakl, C., Somot, S., Aalbers, E., Christensen, O.B., Ciarlò, J.M., Demory, M.-E., Giorgi, F.,
664 Jacob, D., Jones, R.G., Keuler, K., Kjellström, E., Lenderink, G., Levavasseur, G., Nikulin, G., Sillmann, J., Solidoro,
665 C., Sørland, S.L., Steger, C., Teichmann, C., Warrach-Sagi, K., Wulfmeyer, V., 2020. Evaluation of the large EURO-
666 CORDEX regional climate model ensemble. *J. Geophys. Res. Atmospheres* n/a, e2019JD032344.
667 <https://doi.org/10.1029/2019JD032344>

668 Wu, J., Gao, X., 2020. Present day bias and future change signal of temperature over China in a series of multi-GCM driven RCM
669 simulations. *Clim. Dyn.* 54, 1113–1130. <https://doi.org/10.1007/s00382-019-05047-x>

670

671

672

673

674

675

676

677

678

679

680

681

682

683

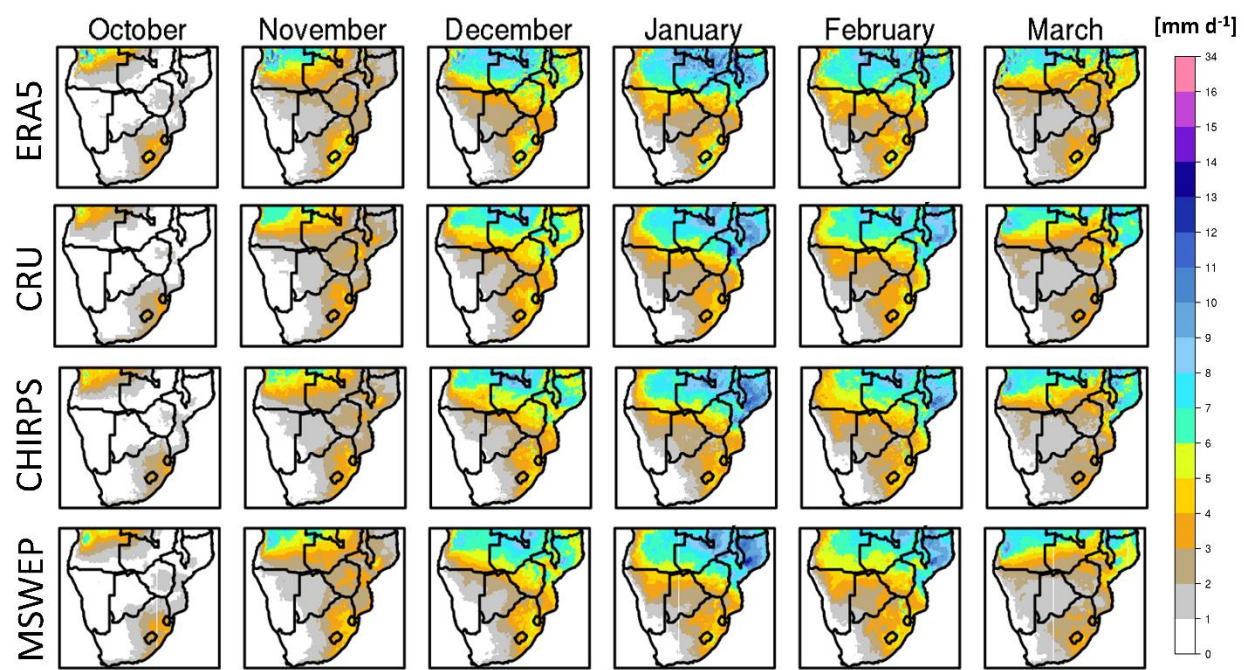
684

685

686

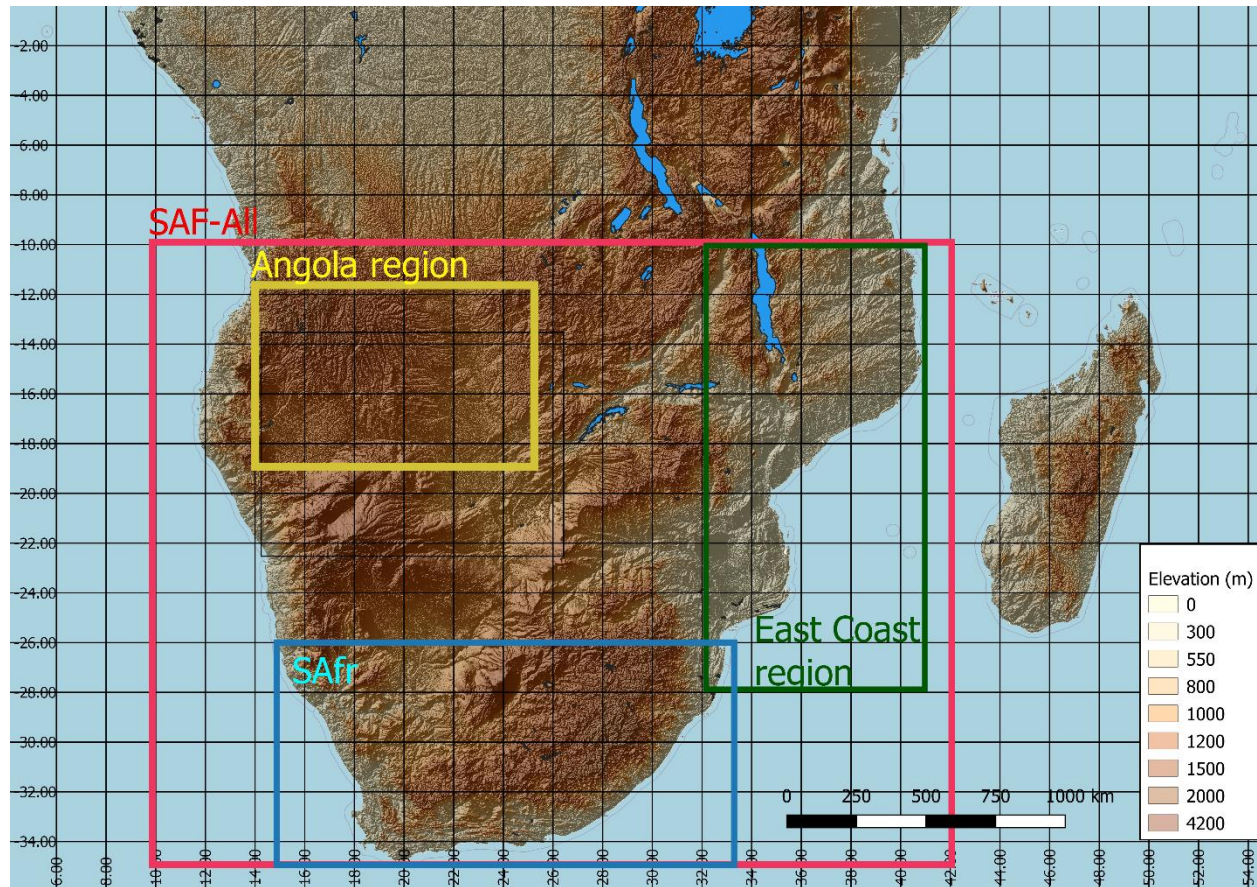
687

688



689

690 **Figure 1.** Monthly mean precipitation climatology for the period 1985-2005.



691

692 **Figure 2.** Study region and subregions over southern Africa.

693

694

695

696

697

698

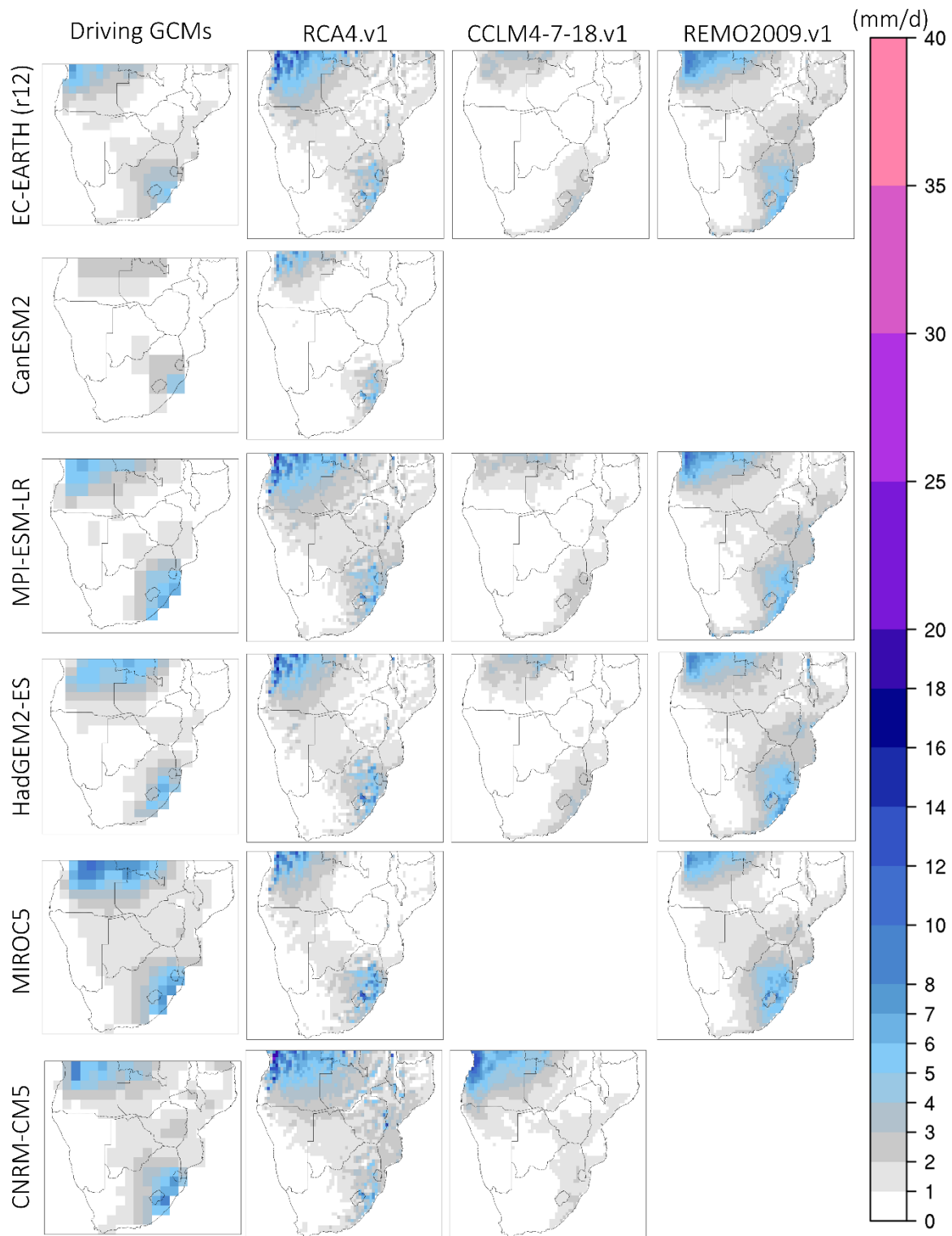
699

700

701

702

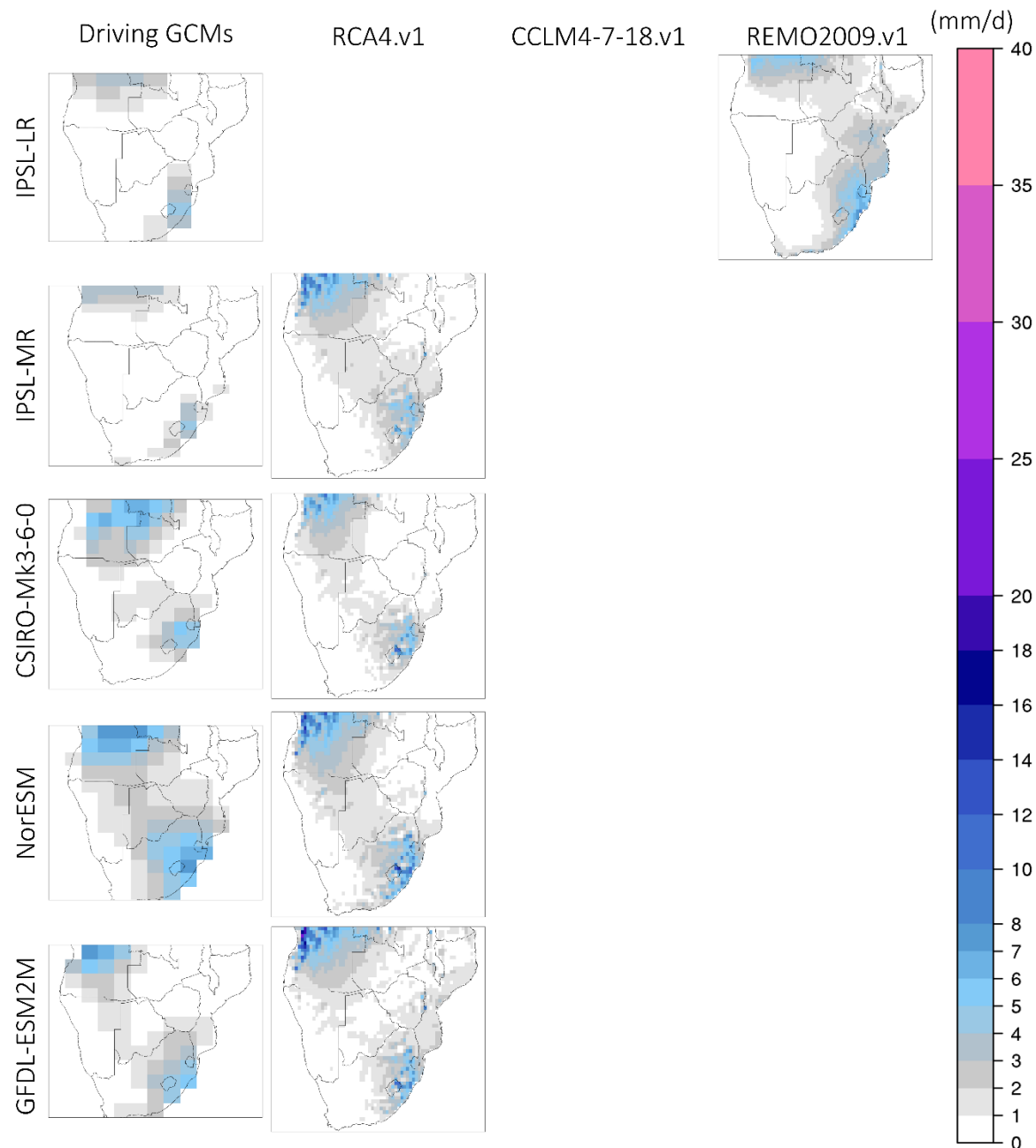
703



704

705 **Figure 3.** Monthly precipitation climatologies (mm/d) during October for the period 1985-2005. First column (from
 706 the left) displays precipitation from the driving GCMs and columns 2-4 display the downscaled precipitation output
 707 from RCA4.v1, CCLM4-8-17.v1 and REMO2009.v1.

708



709

710 **Figure 3.** Continued.

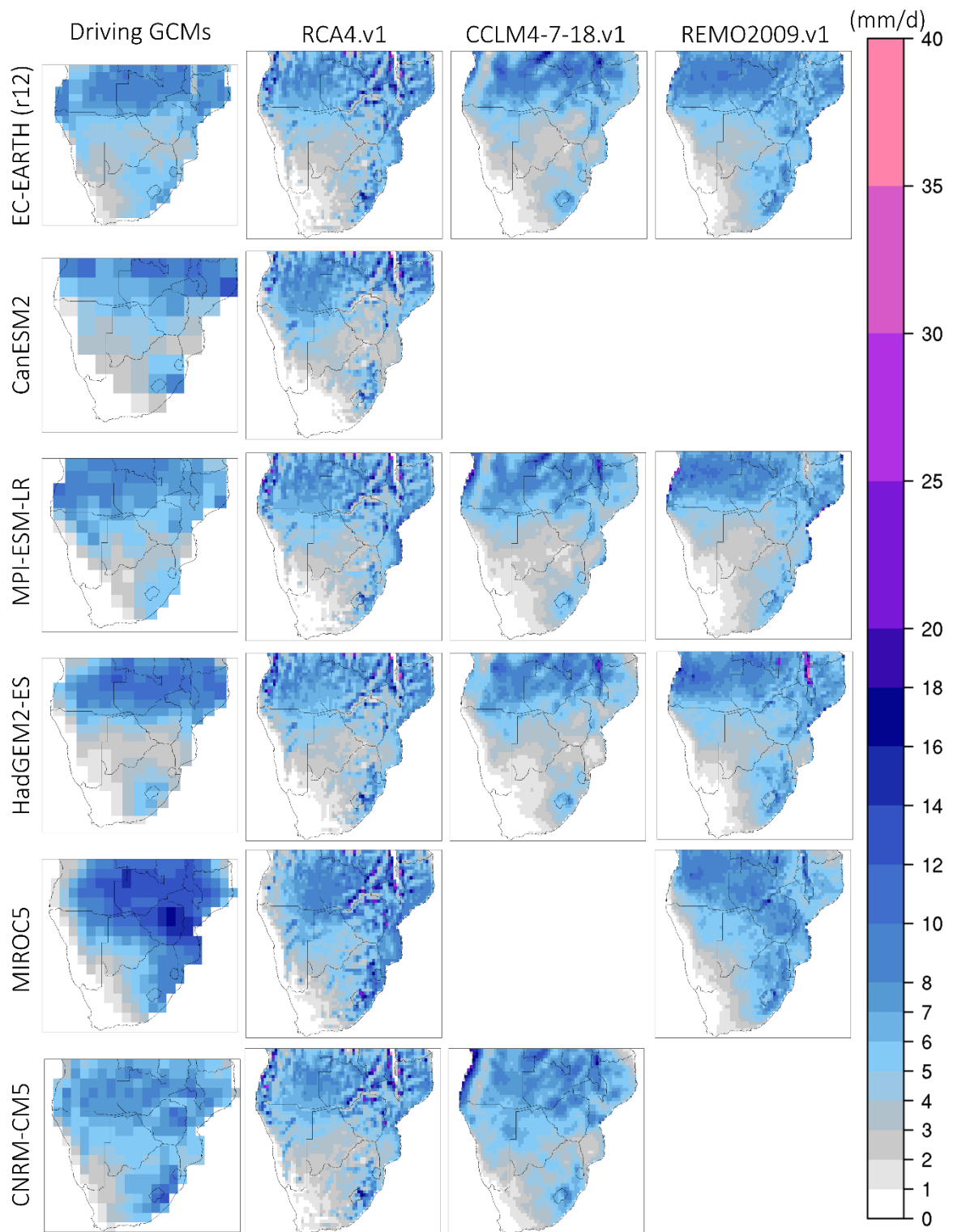
711

712

713

714

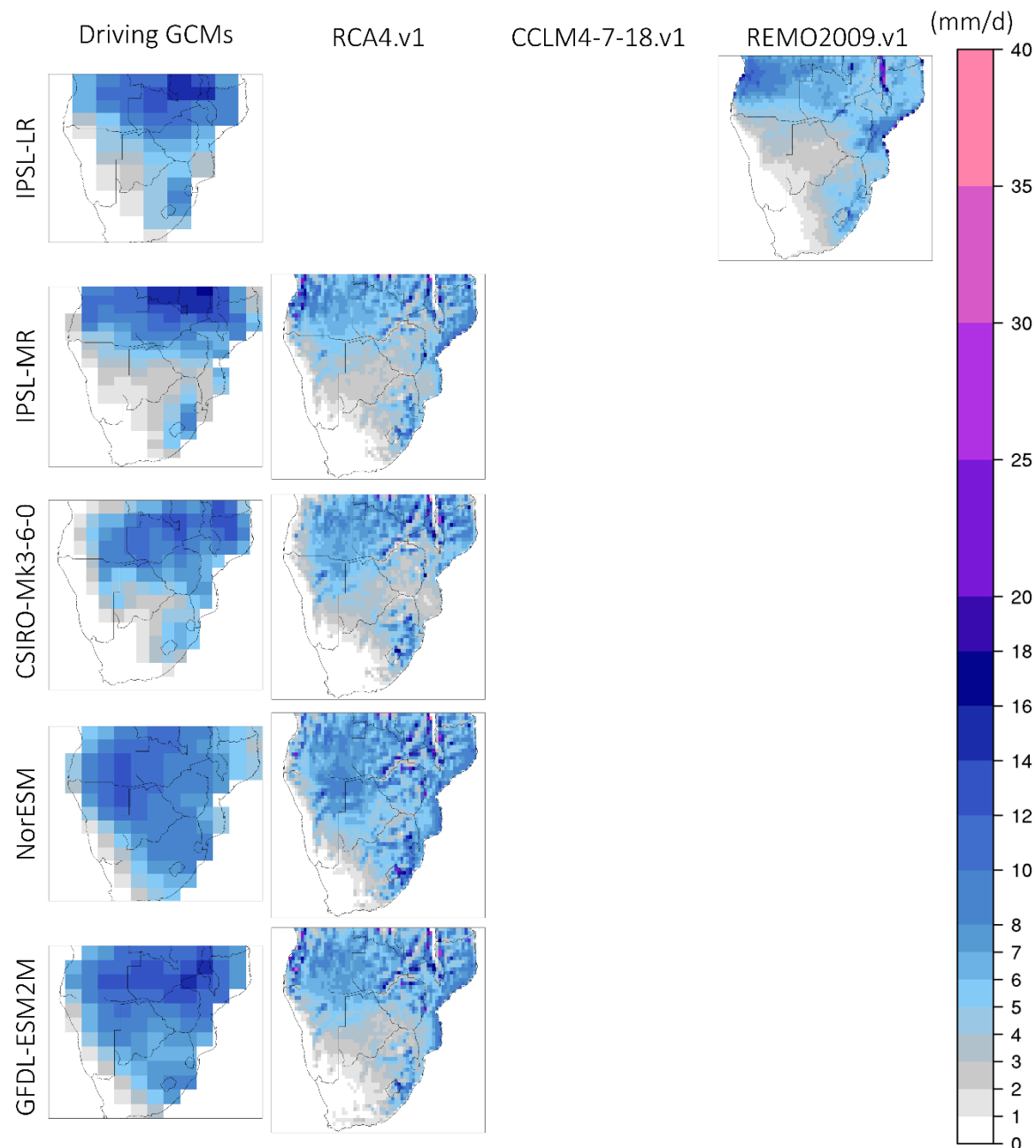
715



716

717 **Figure 4.** Monthly precipitation climatologies (mm/d) during January for the period 1985-2005. First column (from
 718 the left) displays precipitation from the driving GCMs and columns 2-4 display the downscaled precipitation output
 719 from RCA4.v1, CCLM4-8-17.v1 and REMO2009.v1.

720



721

722 **Figure 4.** Continued.

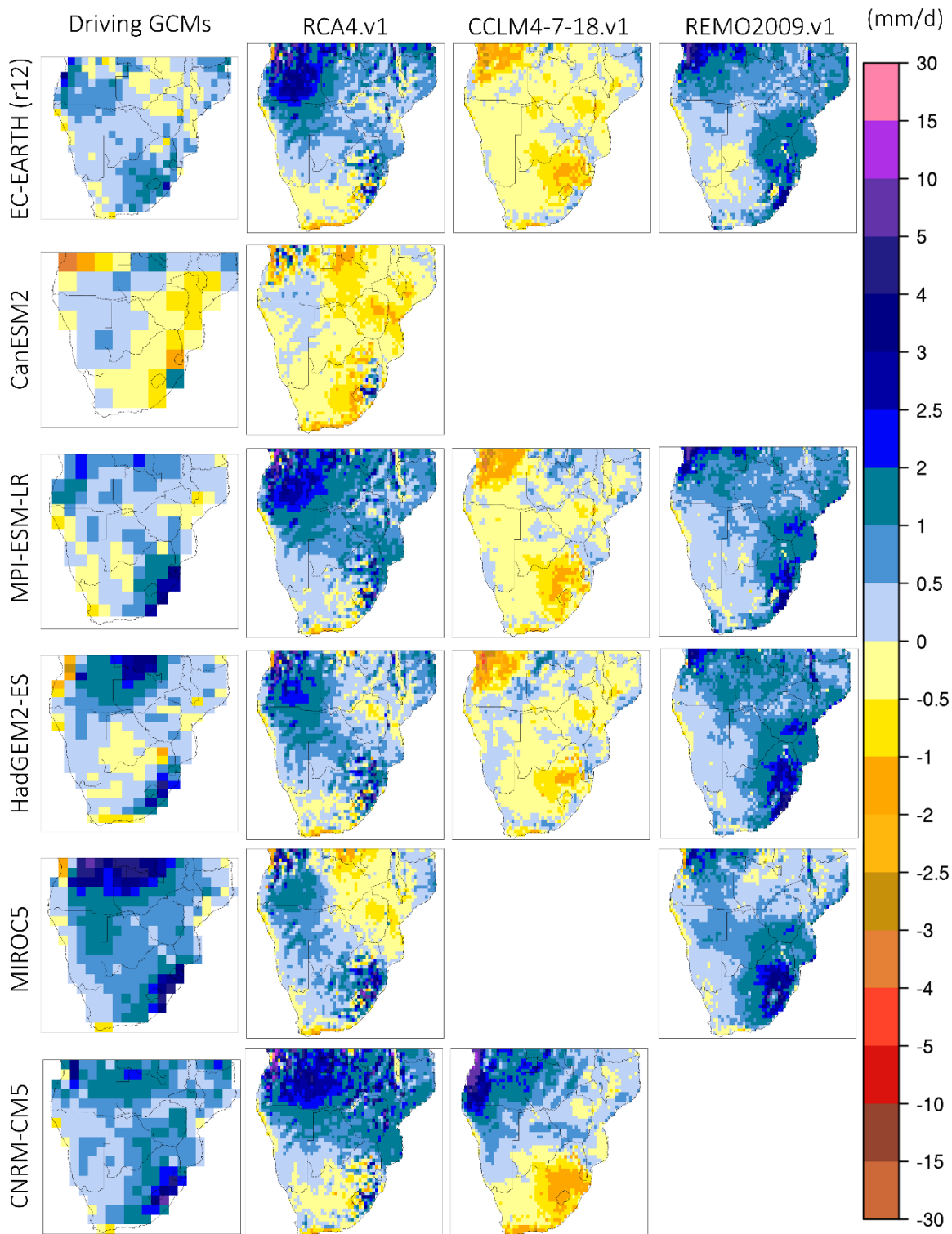
723

724

725

726

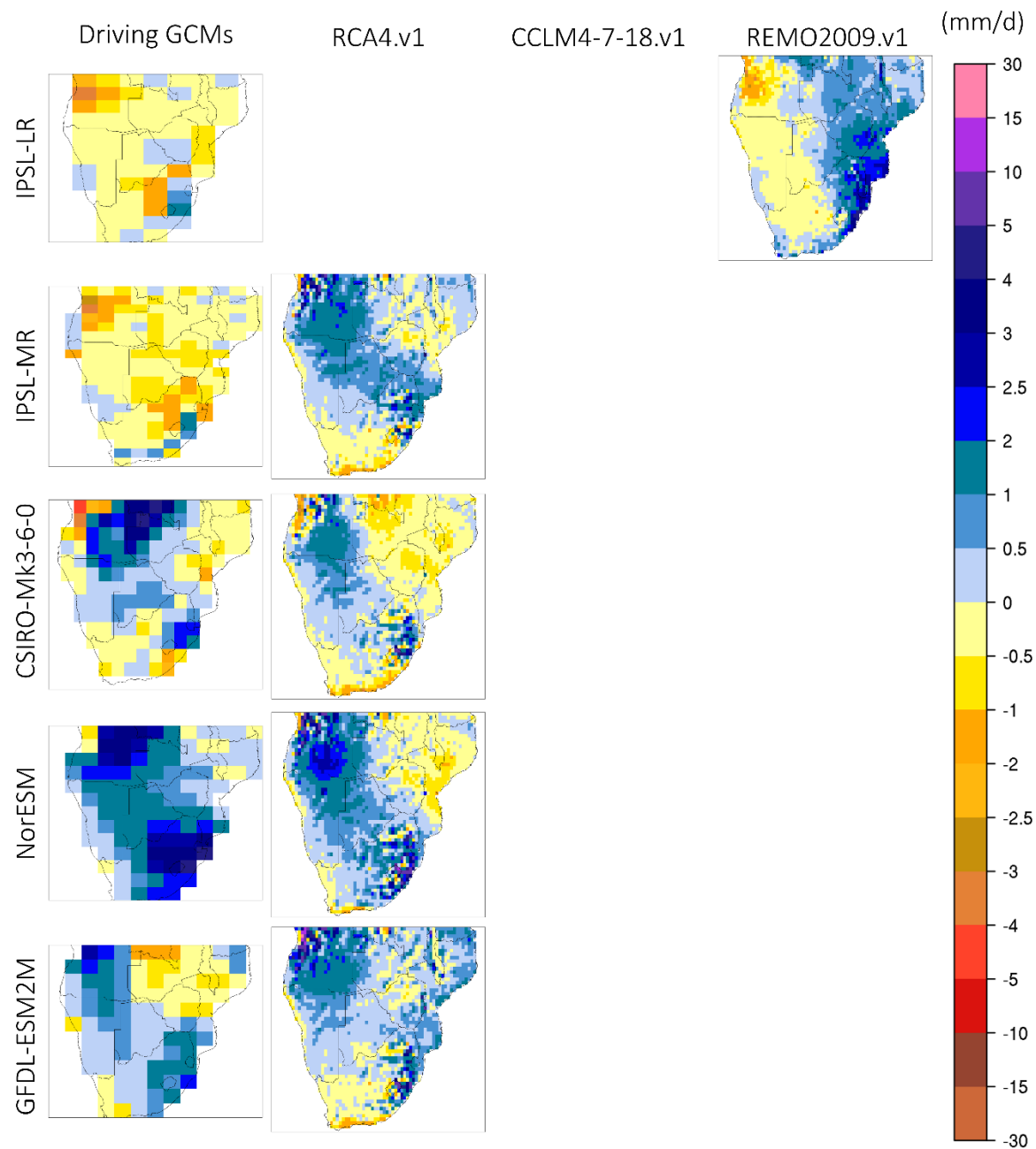
727



728

729 **Figure 5.** Monthly precipitation bias (model – CHIRPS in mm/d) during October for the period 1985-2005. First
 730 column (from the left) displays the biases in the driving GCMs and columns 2-4 display the biases in the downscaled
 731 precipitation output according to RCA4.v1, CCLM4-8-17.v1 and REMO2009.v1.

732



733

734 **Figure 5.** Continued.

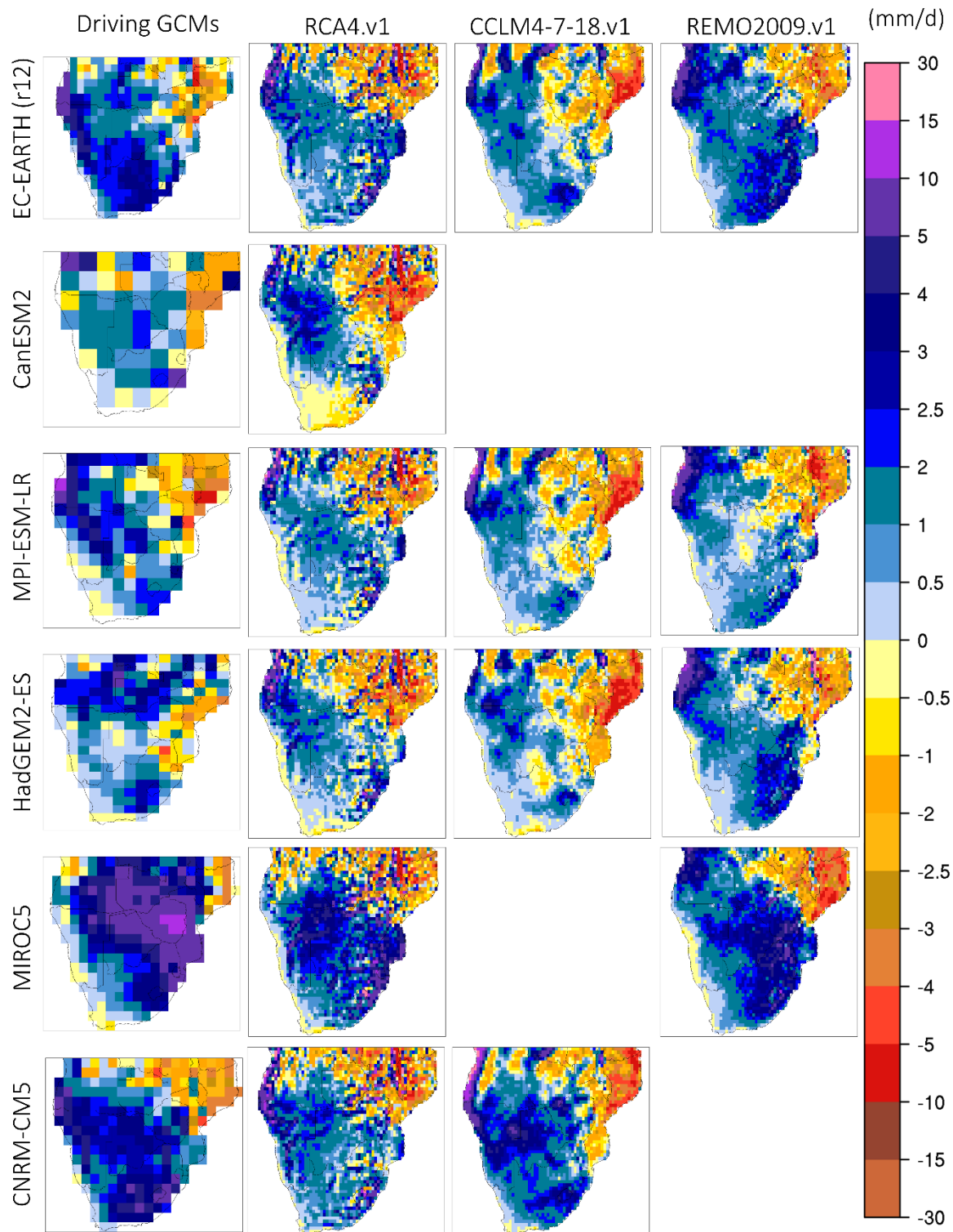
735

736

737

738

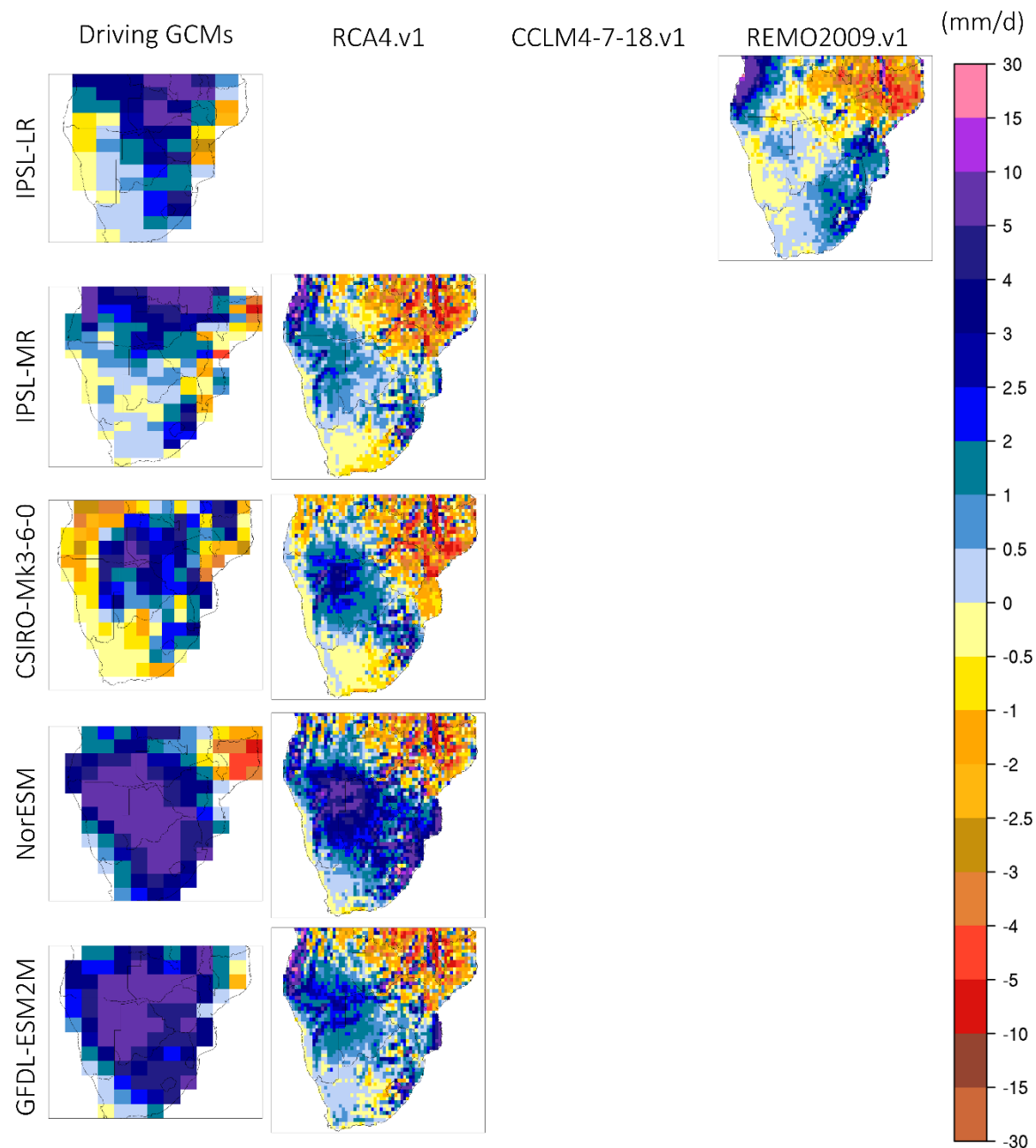
739



740

741 **Figure 6.** Monthly precipitation biases (model – CHIRPS in mm/d) during January for the period 1985-2005. First
 742 column (from the left) displays precipitation biases from the driving GCMs used and columns 2-4 display the
 743 downscaled products according to RCA4.v1, CCLM4-8-17.v1 and REMO2009.v1.

744



745

746 **Figure 6.** Continued.

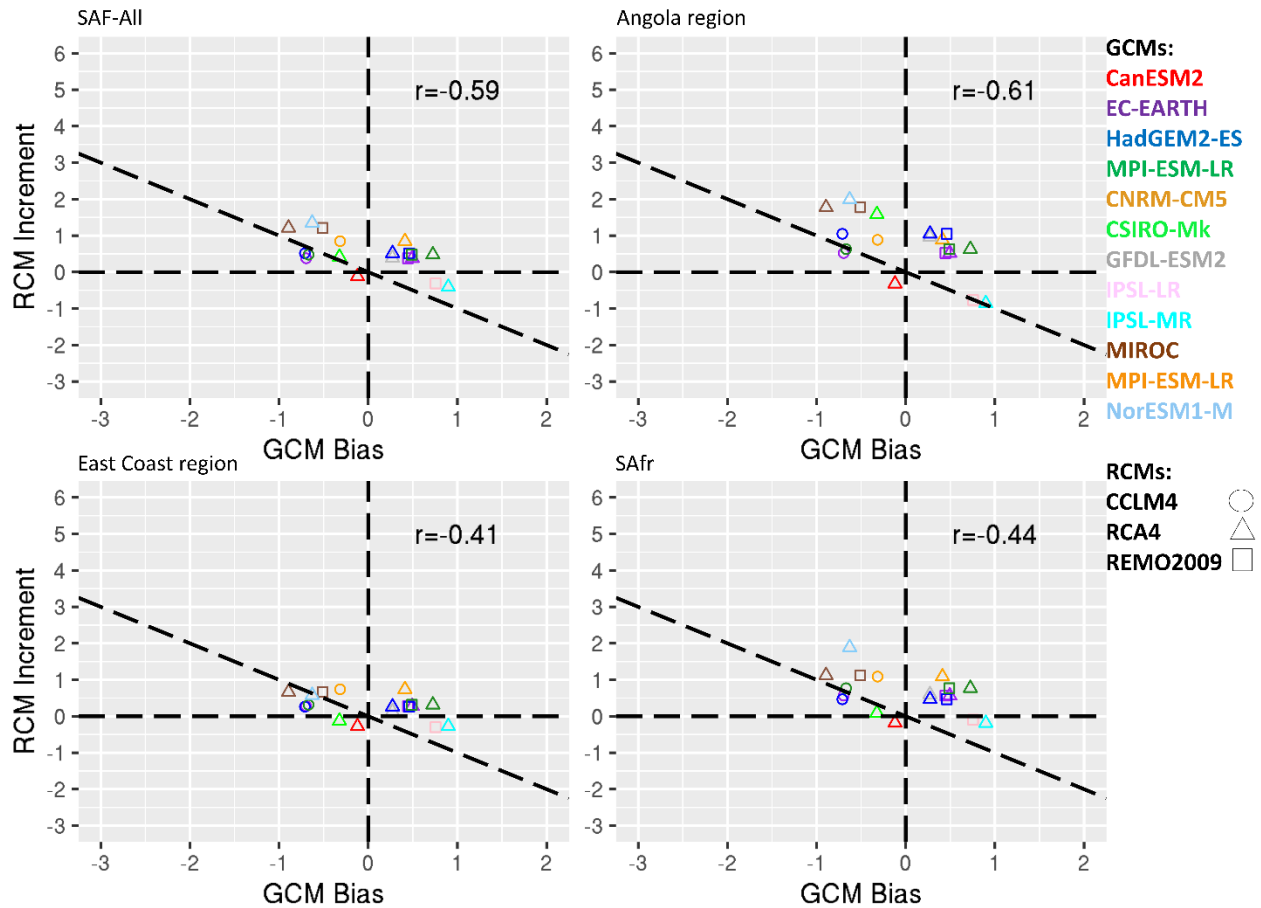
747

748

749

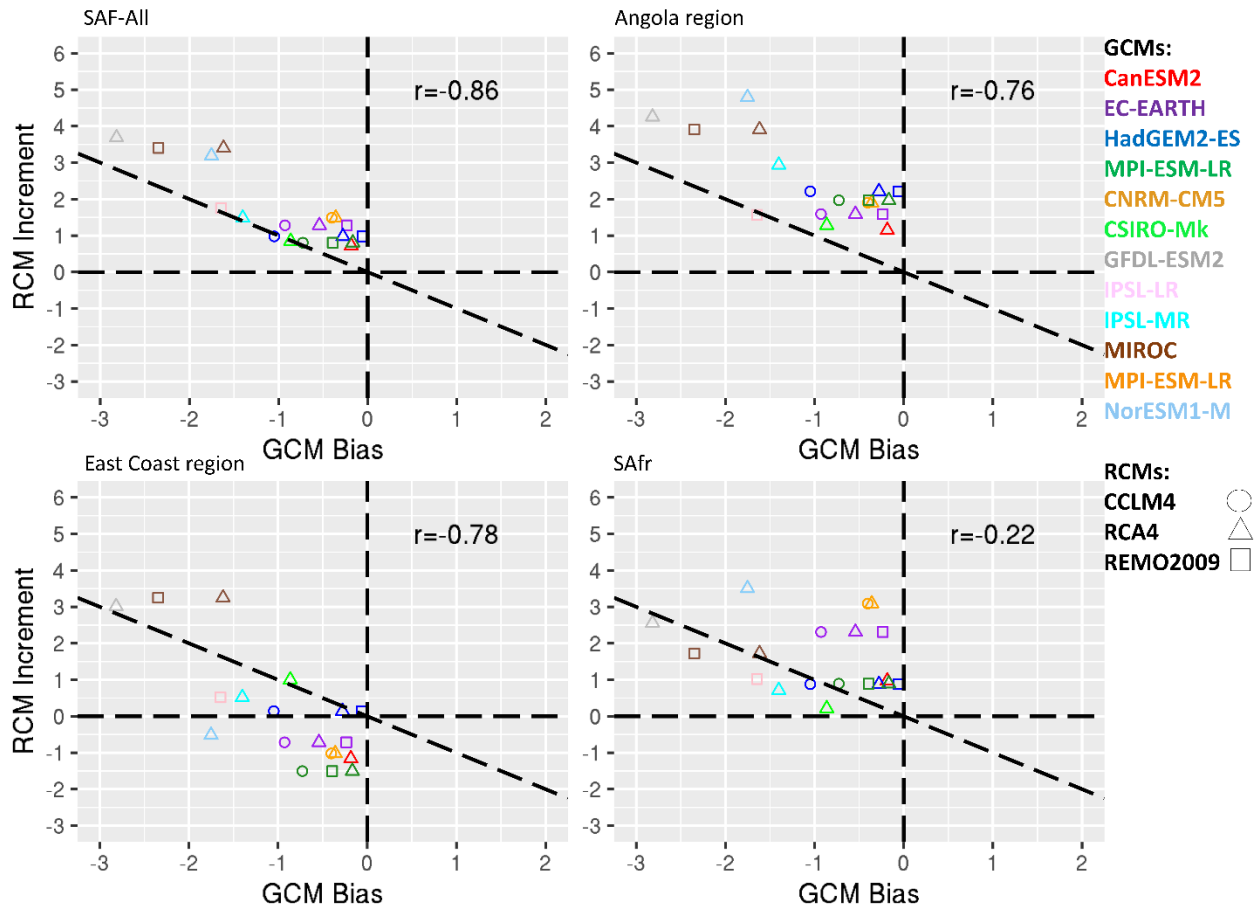
750

751



752

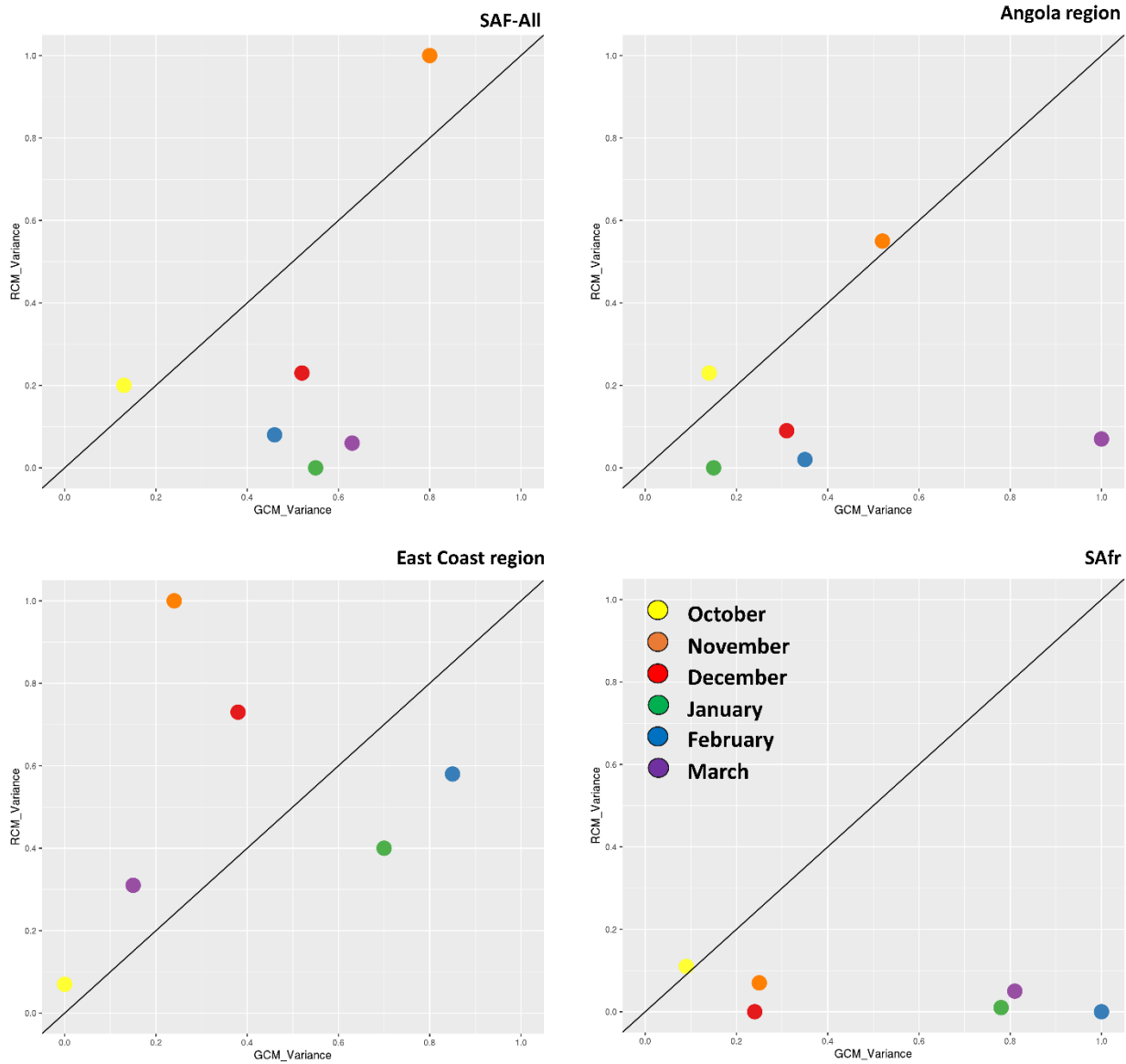
753 **Figure 7.** Scatterplots of the RCM increment (RCM-GCM) for precipitation (mm/day) as a function of the GCM bias
 754 (GCM-OBS) for October. Colors indicate the driving GCM and shapes indicate the downscaling RCMs. The four
 755 panels indicate spatial averages over southern Africa (SAF-All region), the Angola region, the East Coast region and
 756 the SAfFr region.



757

758 **Figure 8.** Scatterplots of the RCM increment (RCM-GCM) for precipitation (mm/day) as a function of the GCM bias
 759 (GCM-OBS) for January. Colors indicate the driving GCM and shapes indicate the downscaling RCMs. The four
 760 panels indicate spatial averages over southern Africa (SAF-All region), the Angola region , the East Coast region and
 761 the SAfr region.

762



763

764 **Figure 9.** Analysis of variance for monthly precipitation during 1985-2005 for southern Africa (SAF-All region) and
 765 the 3 sub-regions examined, namely the Angola region, East Coast region and the SAfr region.. The x and y-axis
 766 display standardized precipitation variances.

767

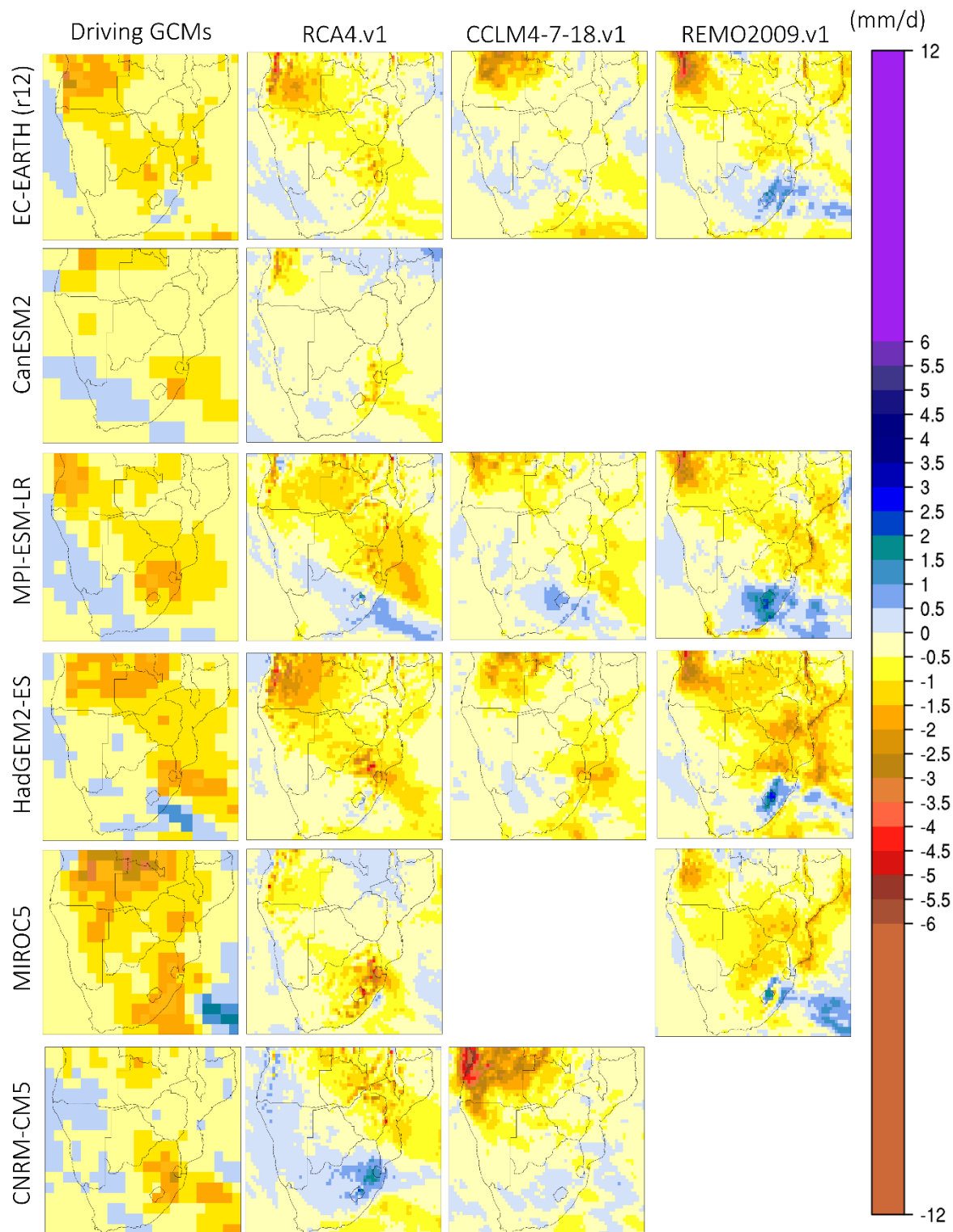
768

769

770

771

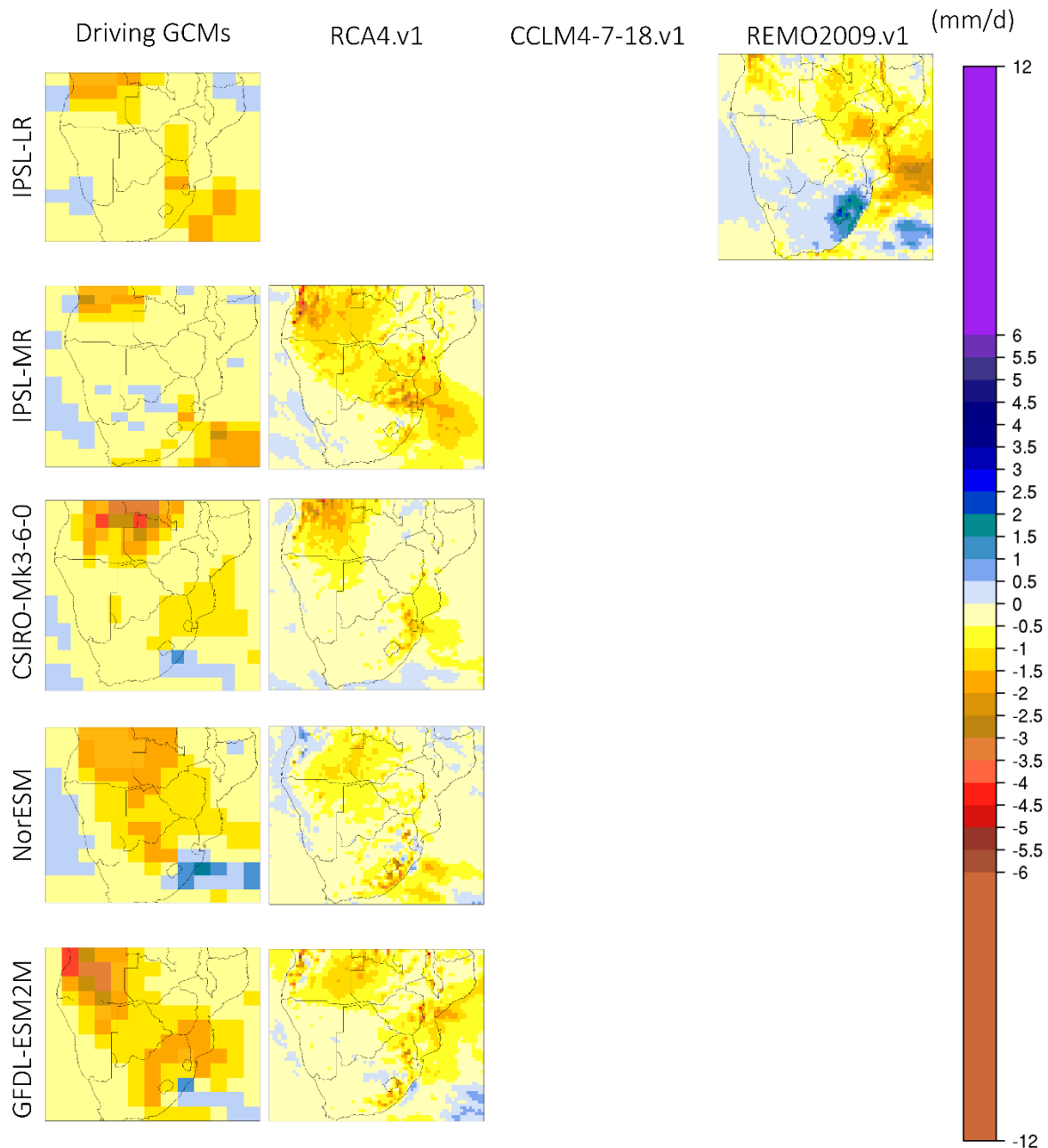
772



773

774 **Figure 10.** Monthly precipitation change (future – present in mm/d) during October for the period 2065-2095 relative
 775 to 1985-2005. First column (from the left) displays precipitation change from the driving GCMs used and columns 2-
 776 4 display the downscaled products according to RCA4.v1, CCLM4-8-17.v1 and REMO2009.v1.

777



778

779 **Figure 10.** Continued.

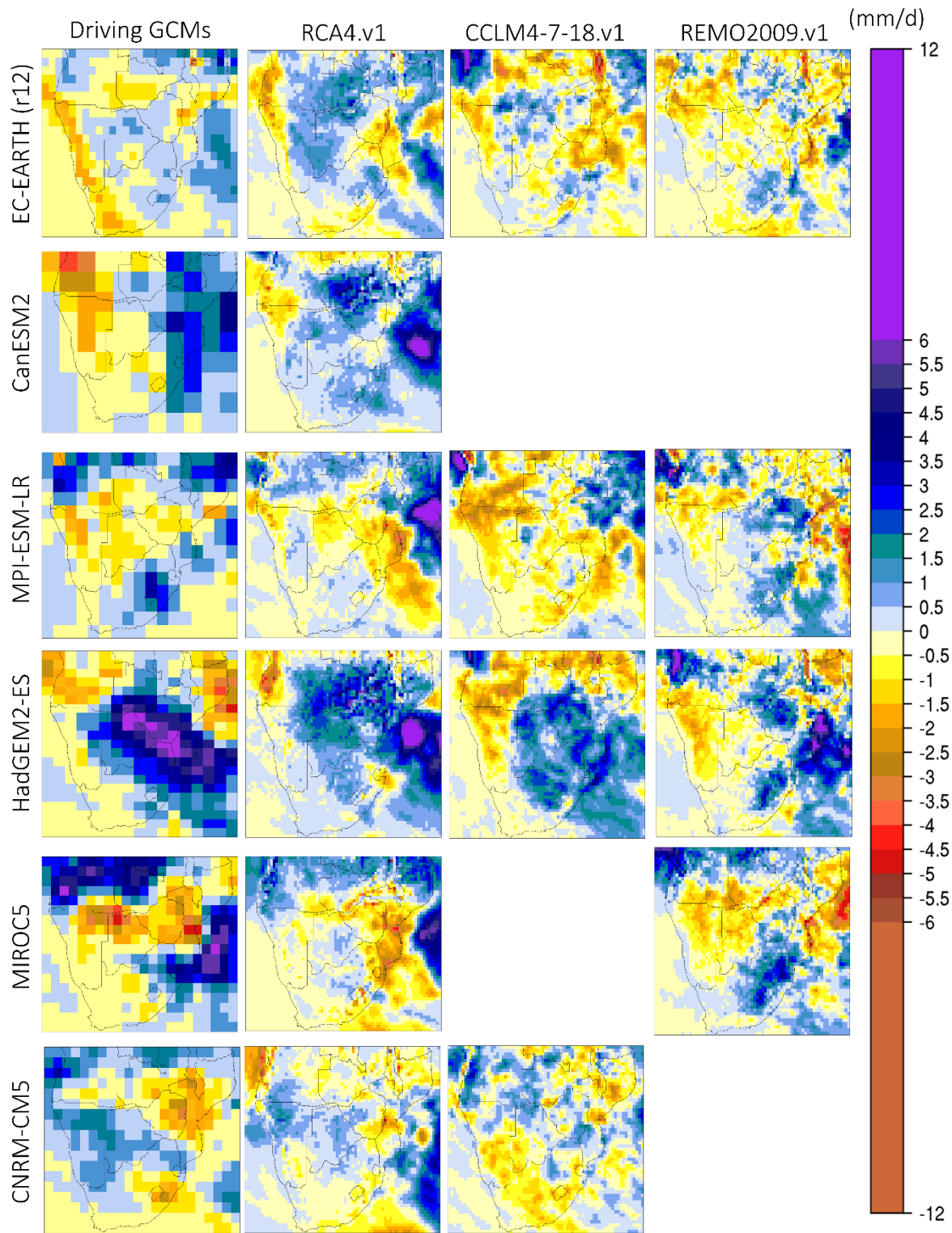
780

781

782

783

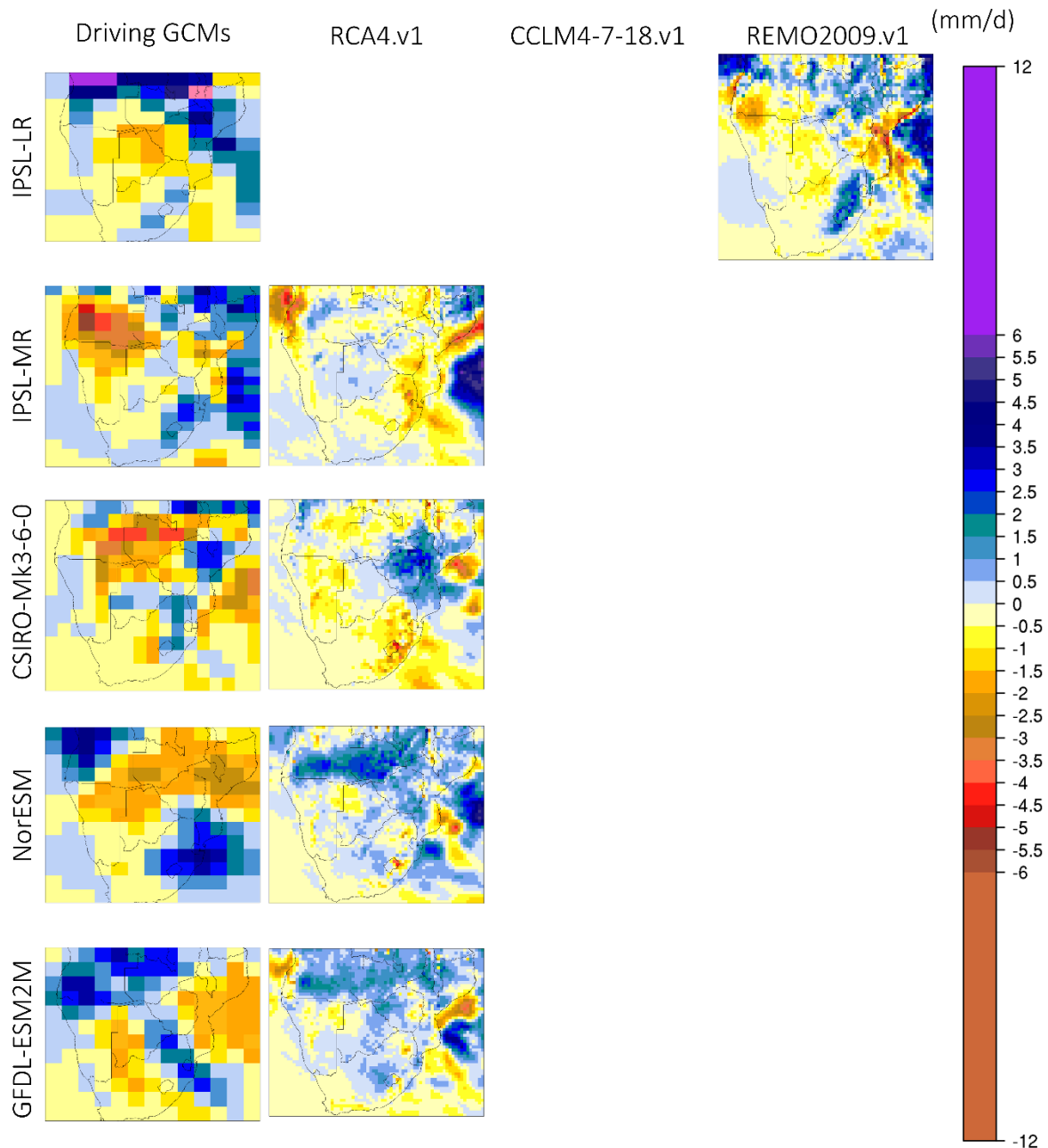
784



785

786 **Figure 11.** Monthly precipitation change (future – present in mm/d) during January for the period 2065-2095 relative
 787 to 1985-2005. First column (from the left) displays precipitation change from the driving GCMs used and columns 2-
 788 4 display the downscaled products according to RCA4.v1, CCLM4-8-17.v1 and REMO2009.v1.

789



790

791 **Figure 11.** Continued.

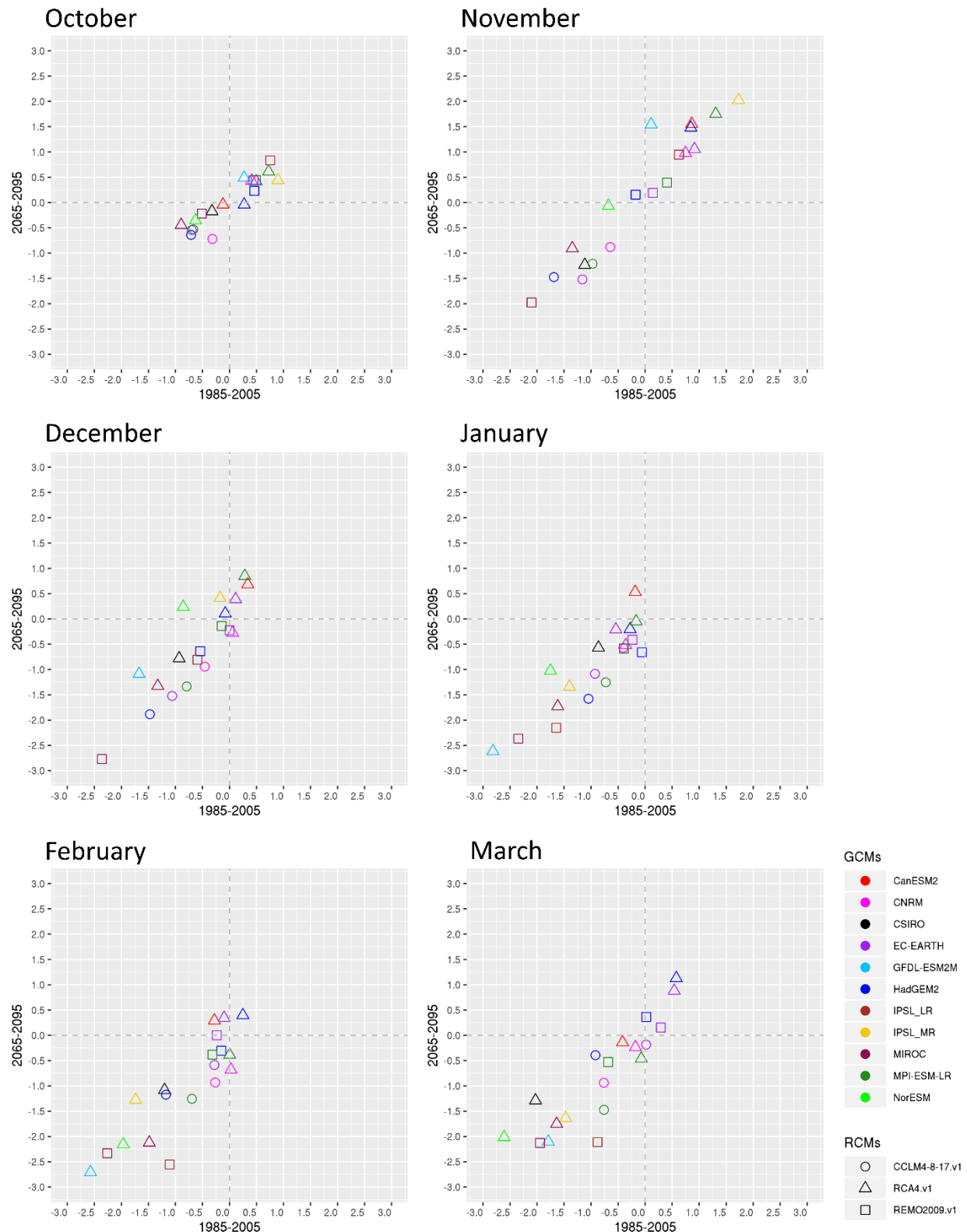
792

793

794

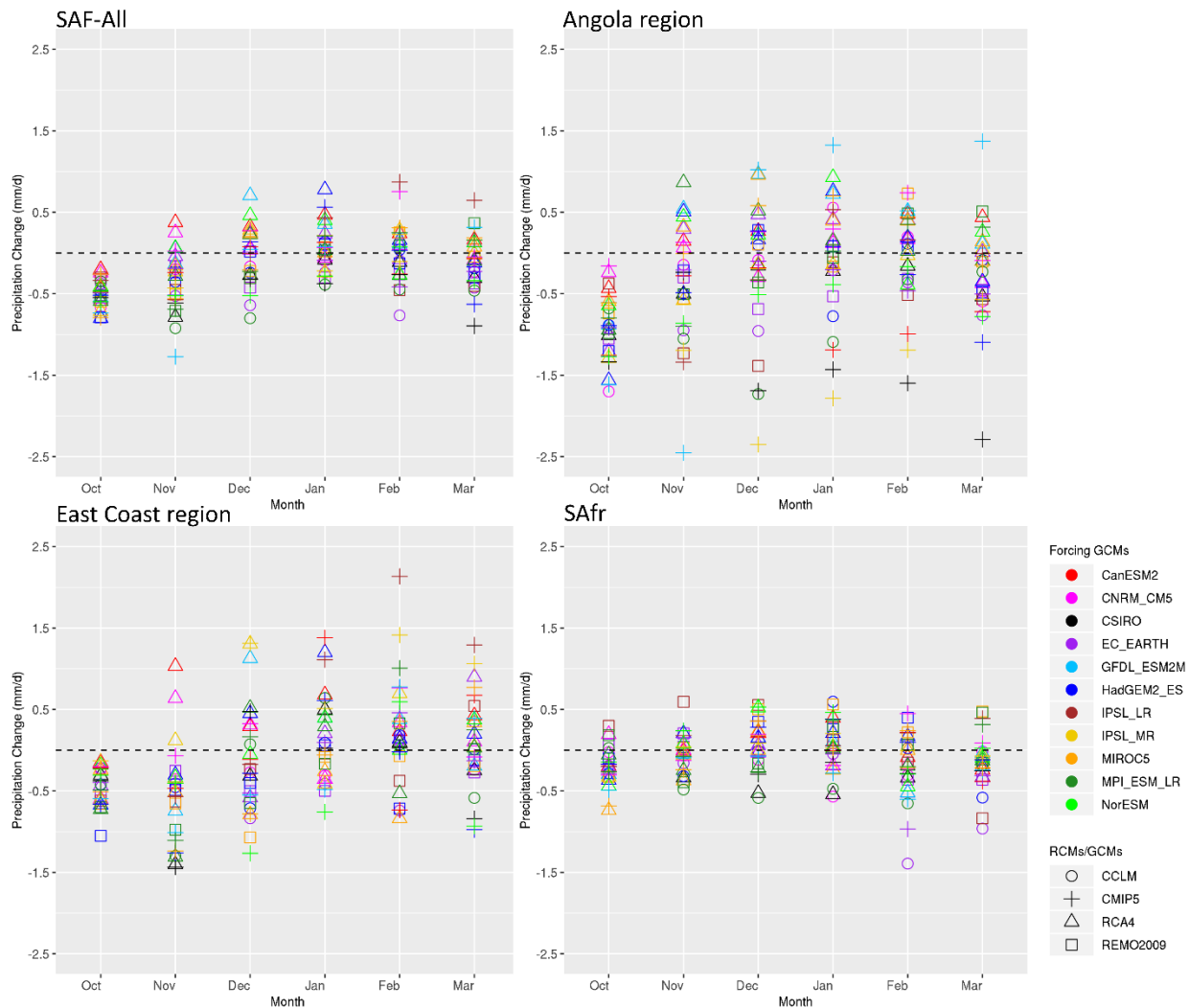
795

796



797

798 **Figure 12.** Monthly RCM_{DRI} – DRI spatial averages over southern Africa for the historical period (1985-2005) on the
 799 x-axis and the future period (2065-2095) under RCP8.5 on the y-axis.



800

801 **Figure 13.** Spatial average of the precipitation change signal (mm/d) from RCMs and their driving GCMs relative to
 802 1985-2005 for southern Africa and the 3 sub-regions examined.

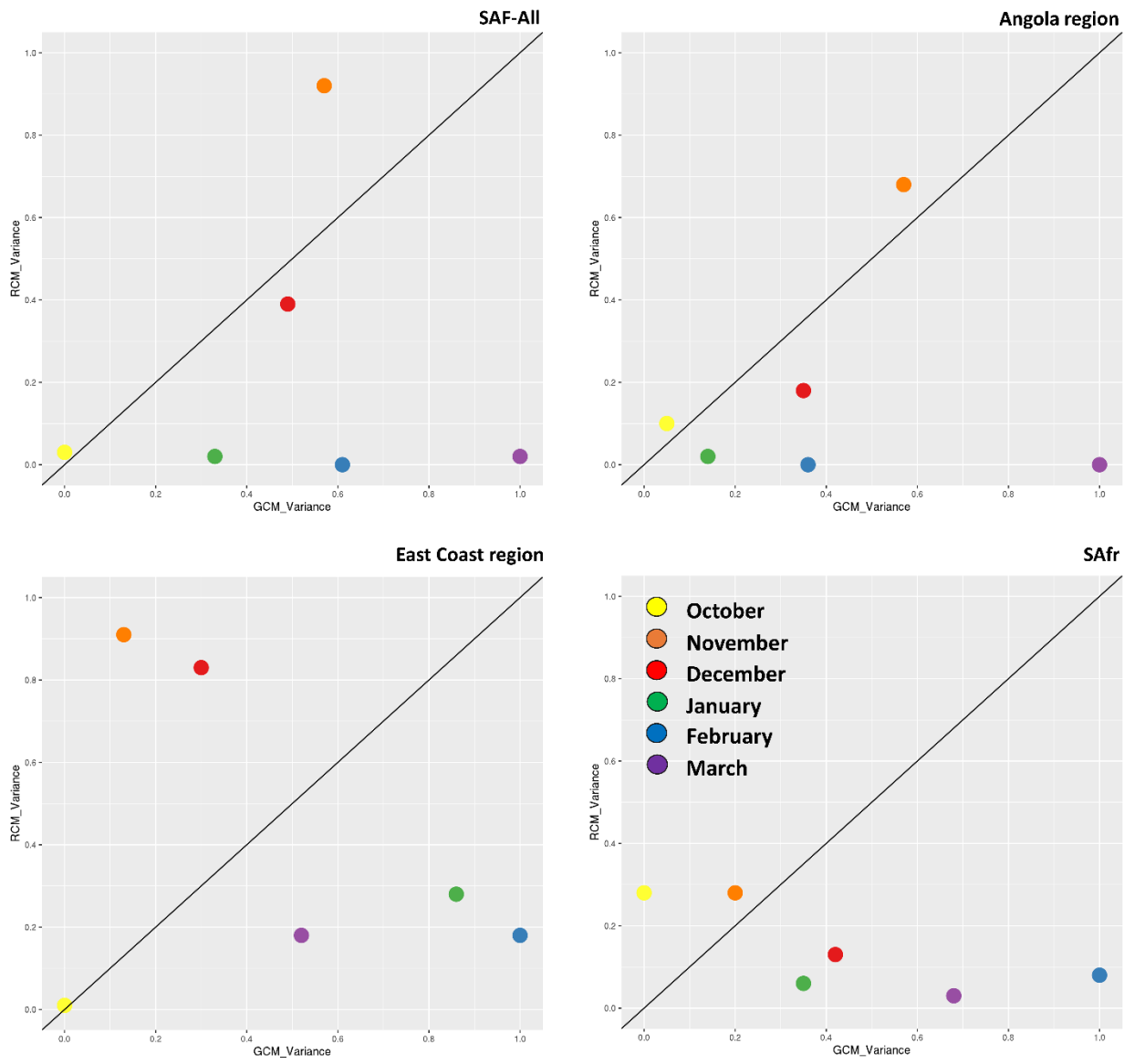


Figure 14. Analysis of variance for monthly precipitation during 2065-2095 for southern Africa (SAF-All region) and the 3 sub-regions examined, namely the Angola region, East Coast region and the SAfr region.. The x and y-axis display standardized precipitation variances.